

JGR Space Physics

RESEARCH ARTICLE

10.1029/2024JA033043

Key Points:

- Ionosphere irregularities are detected during Typhoon Saola, through shipborne ISMR, ground GNSS, HF radar, and SWARM satellite
- Equatorial plasma bubbles are confirmed to exist, causing demonstrable effects on GPS signals and positioning precision
- Neutral winds could aid in propagating atmospheric gravity waves, ultimately intensifying the ionospheric plasma bubbles

Correspondence to:

T. Liu,
tong2.liu@polyu.edu.hk

Citation:

Nie, W., Wang, F., Qiao, Z., Xu, T., Wang, Y., Ye, M., et al. (2024). Ionospheric irregularities coinciding with the 2023 Typhoon Saola: A multi-instrument study. *Journal of Geophysical Research: Space Physics*, 129, e2024JA033043. <https://doi.org/10.1029/2024JA033043>

Received 9 JUL 2024

Accepted 4 DEC 2024

Author Contributions:

Conceptualization: Wenfeng Nie

Data curation: Wenfeng Nie, Lianhuan Hu

Formal analysis: Wenfeng Nie, Fangyuan Wang, Zhizhong Qiao, Yong Wang, Lianhuan Hu

Funding acquisition: Wenfeng Nie, Tianhe Xu

Investigation: Wenfeng Nie, Fangyuan Wang, Yong Wang, Mingzhu Ye

Methodology: Wenfeng Nie

Project administration: Tianhe Xu

Software: Wenfeng Nie

Supervision: Tianhe Xu



Validation: Wenfeng Nie, Zhizhong Qiao

Visualization: Fangyuan Wang, Tong Liu

Writing – original draft: Wenfeng Nie, Fangyuan Wang

Writing – review & editing: Wenfeng Nie, Tong Liu

Ionospheric Irregularities Coinciding With the 2023 Typhoon Saola: A Multi-Instrument Study

Wenfeng Nie¹ , Fangyuan Wang¹ , Zhizhong Qiao¹, Tianhe Xu¹ , Yong Wang¹ , Mingzhu Ye¹, Lianhuan Hu^{2,3} , and Tong Liu⁴ 

¹Shandong Key Laboratory of Optical Astronomy and Solar-Terrestrial Environment, Institute of Space Sciences, Shandong University, Weihai, China, ²Key Laboratory of Earth and Planetary Physics, Institute of Geology and Geophysics, Chinese Academy of Sciences, Beijing, China, ³Beijing National Observatory of Space Environment, Institute of Geology and Geophysics, Chinese Academy of Sciences, Beijing, China, ⁴Department of Land Surveying and Geo-Informatics, The Hong Kong Polytechnic University, Hong Kong, China

Abstract Typhoons exert significant influences on the ionosphere through atmospheric waves, ultimately affecting radio signals in the L-band of the Global Navigation Satellite System (GNSS). Due to the limitations of ground observations, the mechanisms and full impacts of typhoon-induced ionospheric variation remain to be explored. To address this gap, we embarked on a challenging expedition, employing a shipborne ionospheric scintillation monitoring receiver (ISMR) to gather data near the trajectory of Typhoon Saola during August and September 2023. The results revealed prominent amplitude scintillation and total electron content fluctuations in GNSS satellite detections, particularly during sunset from 29 to 31 August 2023. The findings are cross-validated with ground GNSS stations, high-frequency radar and the Swarm satellite, confirming the presence of equatorial plasma bubbles (EPBs). These EPBs have demonstrable effects on GNSS signals, ultimately influencing the precision of positioning performance. By examining the influence of the neutral wind field on atmospheric gravity waves triggered by typhoons, we elucidated how these waves impact the ionosphere, ultimately leading to the formation of plasma bubbles.

Plain Language Summary Typhoons can mess with the radio signals that global navigation systems use by disturbing a part of the atmosphere called the ionosphere. We don't fully understand how this happens because we haven't had enough chances to study it from the land. To fix this, we conducted a shipborne GNSS data collection near Typhoon Saola in August and September 2023 to gather data. We found that the typhoon disrupted satellite signals, especially during sunset, and this led to something called plasma bubbles, which can mess with radio signals and make navigation less accurate. We also looked at how waves in the atmosphere, triggered by the typhoon, caused these bubbles to form. Understanding this helps us figure out how typhoons affect navigation systems, so we can better prepare for signal disruptions during extreme weather.

1. Introduction

Typhoons, also known as tropical cyclones (TC), are powerful cyclonic storms originating in tropical oceans and can profoundly perturb the ionosphere's stability via intricate atmospheric dynamics (Liu et al., 2006). These perturbations have significant implications for the propagation and reception of radio signals, particularly those critical for the Global Navigation Satellite System (GNSS) (Yang & Liu, 2016; Yu & Liu, 2021). To gain a comprehensive understanding of the intricate coupling mechanism between typhoons and the ionosphere and to accurately assess its influence, it is crucial to delve into the detailed characteristics of typhoon-induced ionospheric disturbances.

Typhoons are known for their unique convective system, which includes rotating upwelling and subsiding peripheral flow (Wang & Wu, 2004). This system enables typhoons to continually accumulate energy and moisture, leading to the development of robust convective systems (Anthes, 1974). These convective systems have a high likelihood of generating atmospheric gravity waves (Hines, 1960), which are prevalent in tropospheric regions surrounding the typhoon's trajectory. These gravity waves have expansive wavelengths spanning hundreds of kilometers and can last for several hours. When propagating upward, they eventually reach the upper atmospheric layers, establishing a direct coupling mechanism between typhoons and the ionosphere (Xu et al., 2019).

Since the initial observation of a discernible ionospheric response to hurricane passages (Bauer, 1958), numerous studies have confirmed the significant impact of typhoons on the ionosphere. Evidence of the ability of typhoons to perturb the ionosphere through the generation of acoustic gravity waves was provided by Hung and Kuo (1978) and Tsutsui and Ogawa (1973). A statistical examination of ionospheric acoustic-gravity waves associated with typhoons in Taiwan Island was conducted, utilizing a high frequency (HF) Doppler sounding array (Huang et al., 1985). Then, the propagation characteristics of gravity waves during typhoon passages were analyzed (Hung et al., 1990). Possible evidence of gravity wave coupling with the mid-latitude F region ionosphere was provided by Taylor et al. (1998), and was confirmed by Liu et al. (2006). Chernogor et al. (2022) further demonstrated the ionospheric disturbance launched accompanied typhoon Faxai. Regarding the specific question posed by Li et al. (2022) on how gravity waves triggered by a typhoon propagate from the troposphere to the upper atmosphere, existing research suggests that these waves could propagate vertically, ascending toward the ionosphere through the troposphere and stratosphere.

With the development of GNSS technology, ionospheric total electronic content (TEC) imaging base on GNSS data has providing a potential method to get deeper insights into typhoon-induced ionospheric disturbances. Significant progress has been made by some case studies in understanding how typhoons affect traveling ionospheric disturbances (TIDs). For example, Chen et al. (2020, 2024) documented that typhoon-induced TIDs can travel over long distances, leading to ionospheric disruptions on various scales. Similarly, Chou et al. (2017) observed concentric TIDs generated by gravity waves during typhoon events, which were consistent with global GPS scintillation data. Research by Chernogor and Frolov (2013) and Xu et al. (2019) identified these wave-like TIDs as gravity waves, noting their capacity to produce large-scale ionospheric irregularities. Fu and Jin (2023) also highlighted how typhoon-induced gravity waves can excite medium-scale TIDs in the low-latitude ionosphere.

In addition to these case studies, statistical analyses have provided valuable insights into ionospheric disturbances. Song et al. (2017) examined GPS-derived TEC data during multiple typhoon events, consistently demonstrating the presence of TIDs induced by tropical cyclones. Kong et al. (2017) and Li et al. (2024) further explored the link between TID characteristics and typhoon intensity. More recently, Ma et al. (2024) offered compelling evidence of heightened TID activity during typhoons. Collectively, these studies provide evidence on typhoons to generate TIDs.

In contrast to TIDs, which only induce minor TEC variations and typically pose minimal impact on GNSS positioning, ionospheric irregularities induced by such waves, like plasma bubbles, can cause significant signal scattering, leading to signal loss and abrupt error increases of the GNSS users (Kherani et al., 2009; Singh et al., 1997). Hence, ionospheric irregularities associated with typhoons warrant closer examination.

In the absence of typhoons, studies have shown that atmospheric gravity waves (AGWs) could significantly intensify plasma depletion structures that arise along magnetic field lines after sunset over the magnetic equator (Ajith et al., 2020; Hysell et al., 2014). This enhancement of plasma depletion structures contributes to the formation of notable equatorial plasma bubbles (EPBs) (Ghodpage et al., 2024; Rather et al., 2024). As a result, during sunset, the ionospheric TEC undergoes abrupt and substantial fluctuations, frequently surpassing several TECUs. Such drastic ionospheric irregularities can lead to the loss of lock (De Michelis et al., 2022; Lovati et al., 2023; Peng et al., 2021) and carrier phase cycle slips in GNSS signals (Han et al., 2024), thereby significantly compromising the accuracy, availability, and safety of GNSS users.

During typhoons, the mechanism by which AGWs induce EPBs may be intensified. Xiao et al. (2006) has highlighted that the potential impact of typhoons on ionospheric EPBs, suggesting that AGWs play a key role in seeding ionospheric irregularities. The observations of daytime ionospheric disturbances, including GPS scintillations, were notably evident during Typhoon Tembin in 2012 (Xiao et al., 2012). Statistical analyses further support the correlation between the onset of tropical cyclones and ionospheric irregularities, indicating that storm intensity may significantly influence these disturbances (Yang & Liu, 2016). Research of Li et al. (2018) conducted in Australia between 2005 and 2014 using GNSS and FORMOSAT-3/COSMIC data also reported significant fluctuations in TEC, particularly during Typhoon Gillian. During this event, both TEC and the critical frequency of the F2 layer (f_oF_2) decreased around the storm's peak intensity, contrasting with other typhoons where these values typically increased. These anomalies were concentrated at the edges of the storm, suggesting complex interactions between typhoon-induced gravity waves and the ionosphere. Additional studies by Ke et al. (2020) in Southeast and East Asia have reported similar patterns of ionospheric disturbances during

typhoons. Despite these findings, the influence of typhoons on EPBs still need more deep exploration. Notably, Du et al. (2023) pointed out the role of AGWs generated during the dissipation of typhoons in affecting the ionosphere warrants further investigation.

From the GNSS perspective, monitoring typhoon-induced ionospheric irregularities has traditionally hinged on data sourced from ground stations positioned far from the typhoon's path. Given that typhoons typically form over expansive oceanic areas with limited ground station coverage, acquiring close-range observations of these irregularities pose a great challenge. To bridge this gap, we embarked on an ambitious observational expedition during the 2023 Typhoon Saola, leveraging a ship equipped with an Ionospheric Scintillation Monitor Receiver (ISMR). This approach enabled us to gather unprecedented, close-range measurements of typhoon-induced ionospheric irregularities. The ground-based GNSS observations nearby are used for validation and the measurements from the newly installed HF radar are used for cross-validation (Hu et al., 2024; Sun et al., 2024). Additionally, we leveraged the satellite-based in-situ electron density variations captured by the SWARM constellation (Bennett, 2023; Mohandesi et al., 2023).

All the data utilized in the study is introduced in the second section. The third section elaborates on the observations and analysis of typhoon-related ionospheric irregularities, also, with a focus on the GNSS positioning performance during typhoon events. Subsequently, the discussion turns to exploring the correlation between these ionospheric irregularities and neutral winds. Finally, the key issues are summarized.

2. Data

2.1. Tropical Cyclone Data

The data on tropical cyclones is from the global real-time satellite cloud image website (https://rammb-data.cira.colostate.edu/tc_realtime/, namely RAMMB in NOAA). This website provides information such as the time from the typhoon's formation to its demise, the location of the cyclone's center, and its intensity in terms of wind speed. The website collects a set of data points every 6 hr. For this study, data from two tropical cyclones, namely Saola and Haikui, were utilized.

The trajectory of TC Saola is shown in Figure 1. TC Saola formed in the northeast of the Philippine Islands on 23 August 2023, and circled counterclockwise on the east side of the Philippine Islands before heading west. It reached its peak intensity as a super typhoon on 30 August 30 and entered the South China Sea. On 1–2 September, it made landfall in mainland China and began to weaken. By 3 September, it weakened into a tropical depression and moved generally southwestward until it dissipated on 5 September.

An additional mention is that another cyclone, Haikui, was also active during the ship navigated near the region. As depicted in Figure 2, TC Haikui originated as a tropical depression in the western Pacific on 29 August 2023 and moved west. It escalated into a typhoon on 2 September and attained its peak intensity as a strong typhoon on 3 September as it neared Taiwan Island. Subsequently, it gradually weakened and was downgraded to a tropical depression on 5 September. When TC Saola drew closer to the ship from 29 to 31 August 2023, the distance between TC Saola and the ship narrowed from approximately 800 km to 340–430 km. During this time, TC Saola was gradually attaining its peak phase (with a wind speed of about 60 m/s), whereas TC Haikui had not yet formed a typhoon and was comparatively weaker (with a wind speed of about 25 m/s). Moreover, TC Haikui remained distant from the ship (spanning approximately 1,400–2,200 km) and did not enter the South China Sea throughout its lifecycle. Therefore, the coupling effect of TC Haikui during this period was minimal and will not be further deliberated in this study.

2.2. Multi-Instrument Observations

As illustrated in Figure 1, the observation dataset encompasses various sources, including shipborne ISMR measurements (marked by blue square), ground GNSS observations (marked by yellow trapezoid), HF radar observations from the Low Latitude Long Range Ionospheric Radar (LARID) stationed in Hainan, China (marked by a magenta triangle), and space-based electron density observations from the Swarm satellite for validating the ionospheric irregularities (marked by the green solid line).

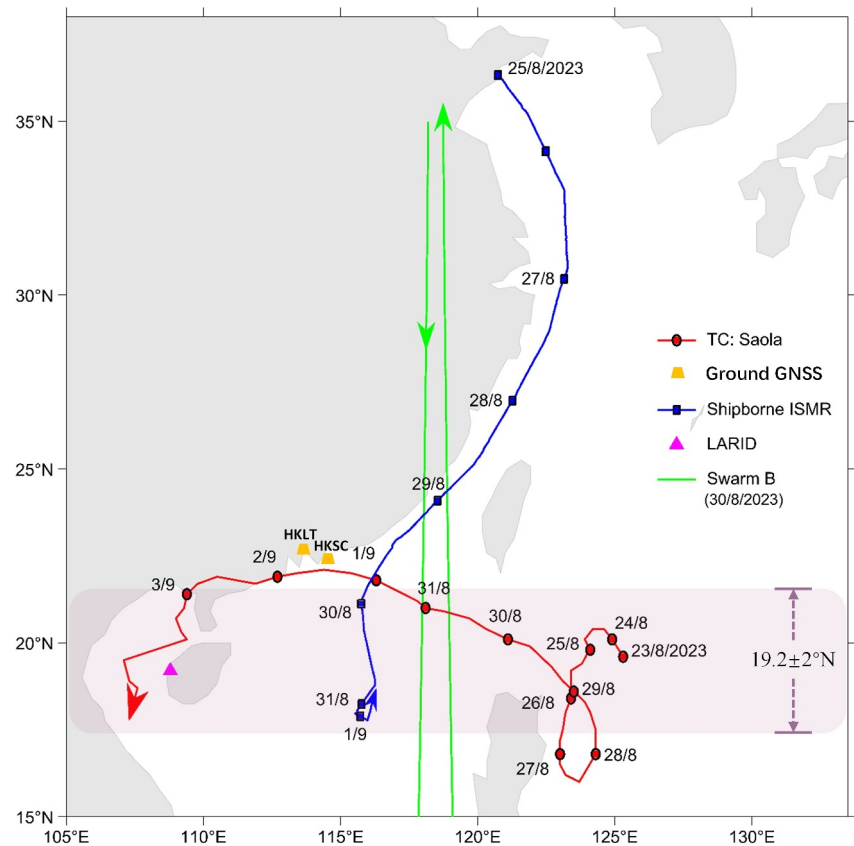


Figure 1. The trajectory of Tropical Cyclone (TC) Saola from 23 August to 3 September 2023. The red trajectory denotes its movement, with the red circular dot signifying the starting point and the position of the cyclone each morning at Universal Time (UT). The blue trajectory depicts the path of the vessel from 25 August to 1 September, with blue square dots marking the vessel's initial position daily. The pink triangle precisely locates the LARID station (incorporating HF radar) in Hainan, China, whose radar beam encompasses a longitude range of approximately $19.2^\circ \pm 2^\circ$, visually represented by a light purple transparent area. The green solid line represents the Swarm satellite's position, exemplified by Swarm B traversing the South China Sea at specific times on 30 August 2023: 12:12 UT northward and 00:48–00:56 UT southward.

2.2.1. Shipborne ISMR Observations and Ground GNSS Observations

The PolaRx5S Ionospheric Scintillation Monitoring Receiver (ISMR) is a high-performance GNSS receiver specifically designed for monitoring ionospheric conditions, including scintillations and TEC variations. It supports measurement outputs at up to 100 Hz, making it well-suited for capturing rapid ionospheric changes. In this study, the shipborne PolaRx5S automatically calculated and recorded amplitude scintillation (S4) and differential TEC (dTEC) with a 60-s time resolution. The elevation cutoff angle was set at 35° , reducing the impact of multipath signals, which are common in marine environments. Advanced filtering techniques in the PolaRx5S further ensure high-quality data, even in the presence of potential radio interference. Figure 3 shows the vessel used to collect ISMR data and the ISMR antenna located on the ship's deck.

As a supplementary observation, raw GNSS data from Hong Kong's Continuously Operating Reference Station (CORS) were used to calculate S4, with HKLT and HKSC stations as examples. The data sampling rate was set to 1 s, and ionospheric pierce points (IPPs) were calculated. IPPs are where GNSS signals intersect the ionosphere at a specific altitude, typically around the F2 peak (approximately 350 km above sea level). Only observations with an elevation angle above 30° were retained.

2.2.2. HF Radar Observations

The Low Latitude Long Range Ionospheric Radar (LARID) in Hainan, China, played a critical role in providing ground-based ionospheric observations (Hu et al., 2024). Operating at a frequency of 20.4 MHz, the radar system

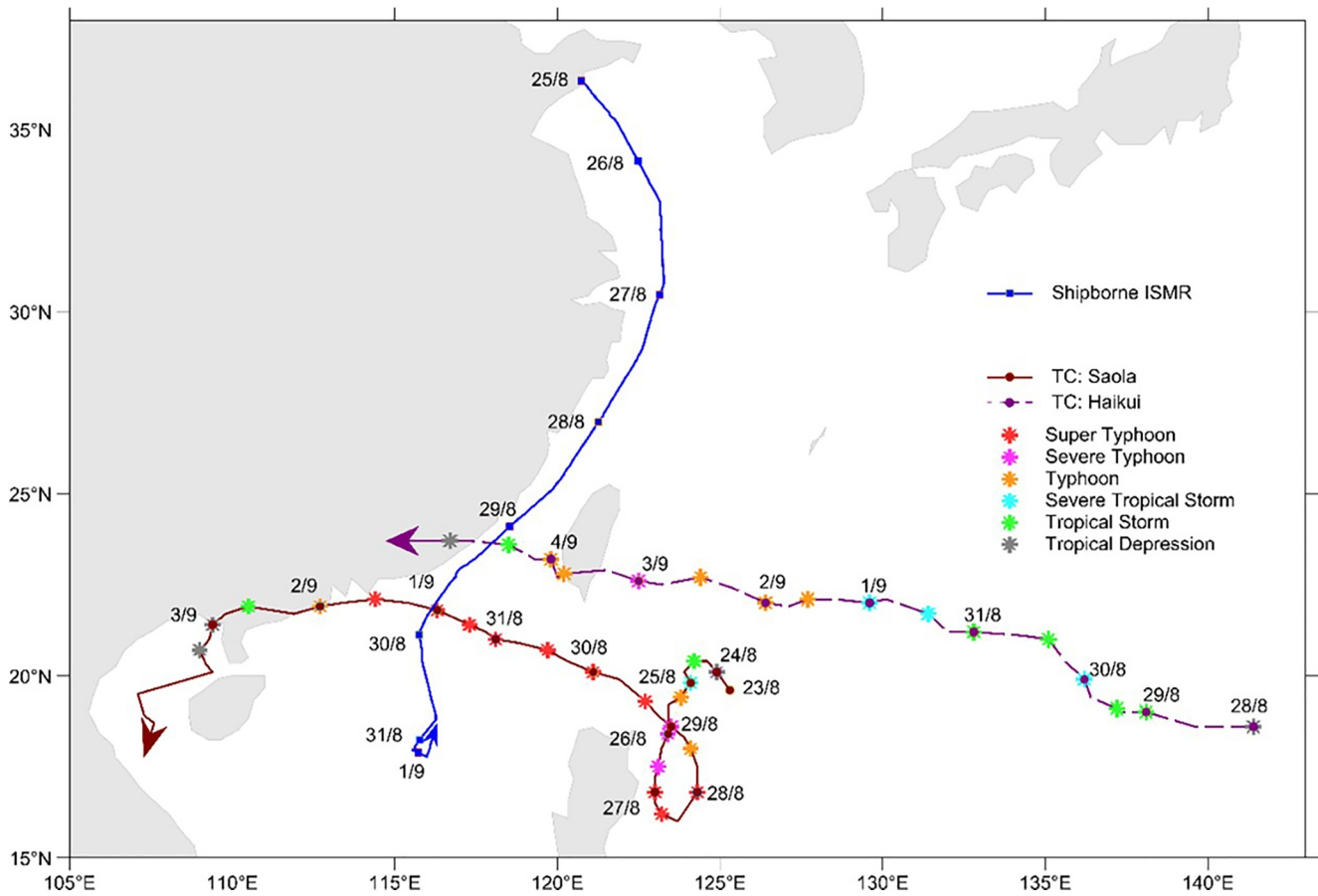


Figure 2. TC Saola (dark red line) from 23 August to 3 September 2023, where the dark red round dot represents the position of TC Saola at 00:00 UT each day. The dark purple dashed line represents the active TC Haikui during roughly the same period, and the dark purple round dot represents the position of TC Haikui at 00:00 UT each day. Stars of different colors indicate different intensity levels of tropical cyclones, as shown in the legend. The blue line represents the position of the ship from 25 August to 1 September 2023, and the blue square point represents the position of the receiving ship at 00:00 UT each day.

alternates between east- and west-looking modes every 2 min, with a total cycle time of 4 min. LARID's range gate extends up to 4,500 km, covering a large region of interest. The center beam's backscattered echo was analyzed, with key parameters such as the signal-to-noise ratio (SNR) and Doppler velocity extracted for identifying plasma irregularities.

2.2.3. Swarm Satellite Observations

To cross-validate the ground-based observations, space-based electron density measurements were obtained from the Swarm satellite (Wood et al., 2022; Xiong et al., 2016). The satellite uses the Electric Field Instrument (EFI)

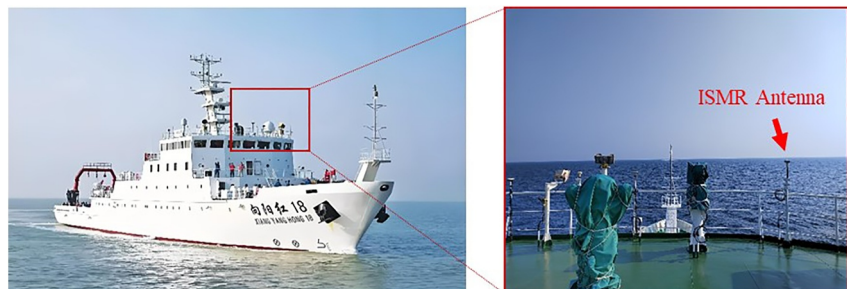


Figure 3. The vessel that used to collect data and the location of the ISMR antenna on the deck.

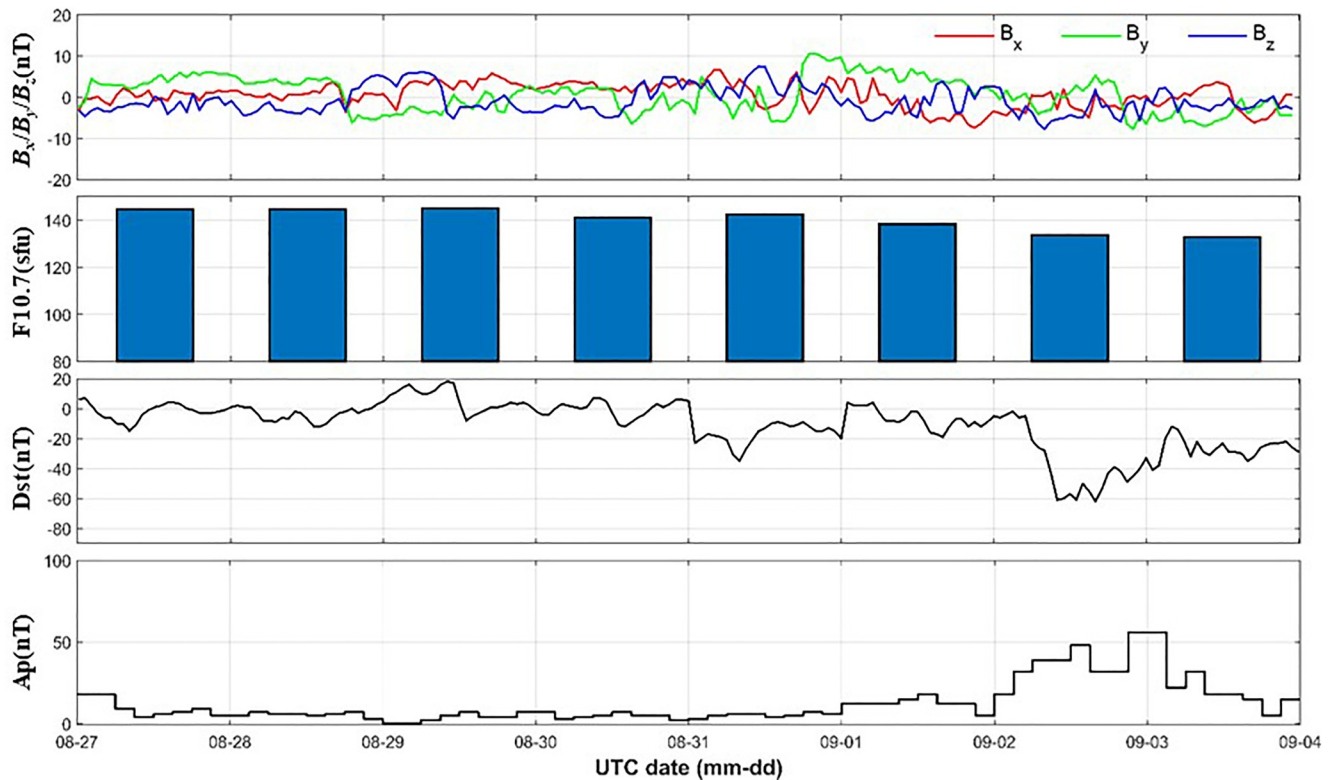


Figure 4. Space weather indexes from 27 August to 4 September 2023. the B_x , B_y , and B_z components of the Interplanetary Magnetic Field (IMF) expressed in the Geocentric Solar Magnetospheric (GSM) coordinate system, denote the magnetic induction intensity along the x , y , and z axes. Additionally, the solar radio flux at 10.7 cm wavelength serves as a crucial metric for quantifying solar radiation intensity. The Dst index reflects the intensity variation of the geomagnetic horizontal component, measured by stations located at mid to low latitudes, offering insights into magnetic storm severity. Lastly, the Ap index, the planetary equivalent three-hour amplitude, encapsulates the global average geomagnetic disturbance intensity over 3 hours. The IMF data are provided from CDAWeb at <https://cdaweb.sci.gsfc.nasa.gov/>. The F10.7 measurement and Dst are provided by the Goddard Space Flight Center (GSFC) from <https://omniweb.gsfc.nasa.gov/>.

Langmuir Probe (LP) to detect plasma density (Ne) at a high frequency of 2 Hz, allowing detailed monitoring of electron density variations. These in-situ observations are crucial for capturing small-scale ionospheric irregularities, such as EPBs. The Swarm satellite's trajectory was synchronized with ISMR and LARID observations, providing direct temporal and spatial comparisons.

2.3. Space Weather Index

As Typhoon Saola moved across the South China Sea, the observed geomagnetic activity intensity experienced minor fluctuations but remained benign, amidst stable solar conditions. Figure 4 showcases the space weather indices spanning from 27 August to 4 September 2023. In this context, Figure 4 depicts a period of remarkable geomagnetic stability from 27 August to 2 September, with Ap values fluctuating benignly between 0 and 20, and Dst values remaining within a narrow range of -40 – 2 nT, indicating minimal influence on ionospheric variations (Palacios et al., 2018). Then, a slight escalation in geomagnetic activity was observed on 2–3 September, aligning with the aftermath of Typhoon Saola's landfall. The fluctuations in F10.7, IMF, and Dst indices from 2 to 4 September suggest a moderate level of solar activity after the typhoon's landfall.

3. Observations and Analysis

3.1. GNSS Signal Scintillation During Typhoon Saola

This subsection presents the scintillation of the shipboard receiver and the Hong Kong ground station. The variation of the S4 index over time and across IPP trajectories near the typhoon was examined.

3.1.1. Shipborne ISMR Observations

As depicted in Figure 1, the vessel with ISMR on board, embarked from southern Shandong on 25 August 2023, and subsequently proceeded southwards along the entire eastern coast of China. On 29 August, TC Saola intensified into a super typhoon, and its trajectory brought it within close proximity to the vessel. From 29 to 31 August, our vessel was situated in the vicinity of TC Saola, providing a rare opportunity for ISMR to acquire data on the ionospheric variation induced by TC Saola. Following this, the vessel conducted further observations at $18.44^{\circ}\sim 19.17^{\circ}\text{N}$ and $115.93^{\circ}\sim 116.33^{\circ}\text{E}$.

Figure 5 presents the S4 index and dTEC time series of BeiDou, GPS, GLONASS, and Galileo acquired by the shipborne ISMR during TC Saola's passage. The upper two subplots in Figure 5 demonstrate a substantial increase in S4 and dTEC fluctuations during the sunset hours (around 12:00 UT and the following hours, where $\text{LT} = \text{UT} + 8 \text{ hr}$) when TC Saola approached the vessel from 29 to 31 August 2023. For example, notable fluctuations were observed for BeiDou satellites with Pseudo-Random Noise (PRN) numbers 1–4, designated as C1–C4. Specifically, numerous data points with S4 indices exceeding 0.5 are visible during sunset, with some satellites recording S4 maximum values surpassing 1, and even nearing 1.5. In contrast, during other dates, fluctuations present during sunset are less noticeable than those observed from 29 to 31 August. Notably, the timing and amplitude of scintillation events observed on GPS, GLONASS, and Galileo satellites were almost identical to those of BeiDou satellites.

From 29 to 31 August, during the presence of Super Typhoon Saola and the ship's proximity, dTEC displayed significant fluctuations in the early evening, reaching amplitudes of 1 TECU and, in certain cases, exceeding 1.5 TECU. As depicted in the upper panel of Figure 5b, satellites C5, C6, C8, C9, C13, and C16 exhibited a clear increase in S4 fluctuations during sunset from 29 to 31 August.

These enhanced S4 and dTEC fluctuations during sunset hours from 29 to 31 August typically persisted for over 3 hr, with a duration of almost 6 hr. During the sunset hours of 27–28 August, when the ship was further away from the typhoon, the duration of S4 and dTEC fluctuations on the C1 and C4 satellites was short (around 1 hr) and did not seem to be associated with the typhoon's passage, in contrast to the fluctuations observed from 29 to 31 August.

As seen in the bottom of Figure 5, similar to the BeiDou satellites, certain GPS satellites also displayed intensified fluctuations during sunset from 29 to 31 August. Among these, G2, G8, G16, G27, G31, and G32 exhibited the most notable enhancements.

Figure 6 depicts the IPPs along with S4 and dTEC for the satellites notably impacted by enhanced fluctuations at sunset, as observed by the shipborne ISMR on 30 August 2023. The trajectories of different BeiDou and GPS satellites are presented based on the 350 km thin shell approximation (Klobuchar, 1987). As TC Saola approached the ship, a significant enhancement in ionospheric irregularities was observed near sunset in the vicinity of the ship. From the locations where S4 and dTEC fluctuations observed by BeiDou's geostationary Earth orbit (GEO) satellites and GPS's medium Earth orbit (MEO) satellites, it is evident that these irregularities occurred in the South China Sea, likely on its eastern side. These irregularities arise near sunset during the autumnal equinox (Sun et al., 2016) in China and neighboring low-latitude regions, exhibiting significant variations that persist for several hours.

At this time, the maximum wind speed near the center of Typhoon Saola exceeded 17 on the Beaufort scale, corresponding to 62 m/s. The radii of the wind fields were as follows: 220–250 km for the 7-level wind field, 130 km for the 10-level wind field, and 70 km for the 12-level wind field. Prior to sunset, satellites G16, G27, G31, and G32 detected ionospheric scintillation. On 30 August, the IPP mapping points of these satellites were positioned approximately 70 km, 60 km, 15 km, and 60 km from the typhoon's center, respectively. This observation suggests that ionospheric scintillation occurred within both the central wind field and the 12-level wind field, independent of any enhancements related to sunset. The scintillation is likely attributable to irregularities induced by the typhoon. During sunset, satellites G2 and G8 detected ionospheric scintillation at a latitude of 15°N , further south than the scintillation recorded by the earlier satellites, at approximately 70 km from the typhoon's center. At this stage, the scintillation is more likely the result of pre-existing interactions between the upper atmosphere and the ionosphere, which were intensified during the typhoon, leading to the formation of EPBs.

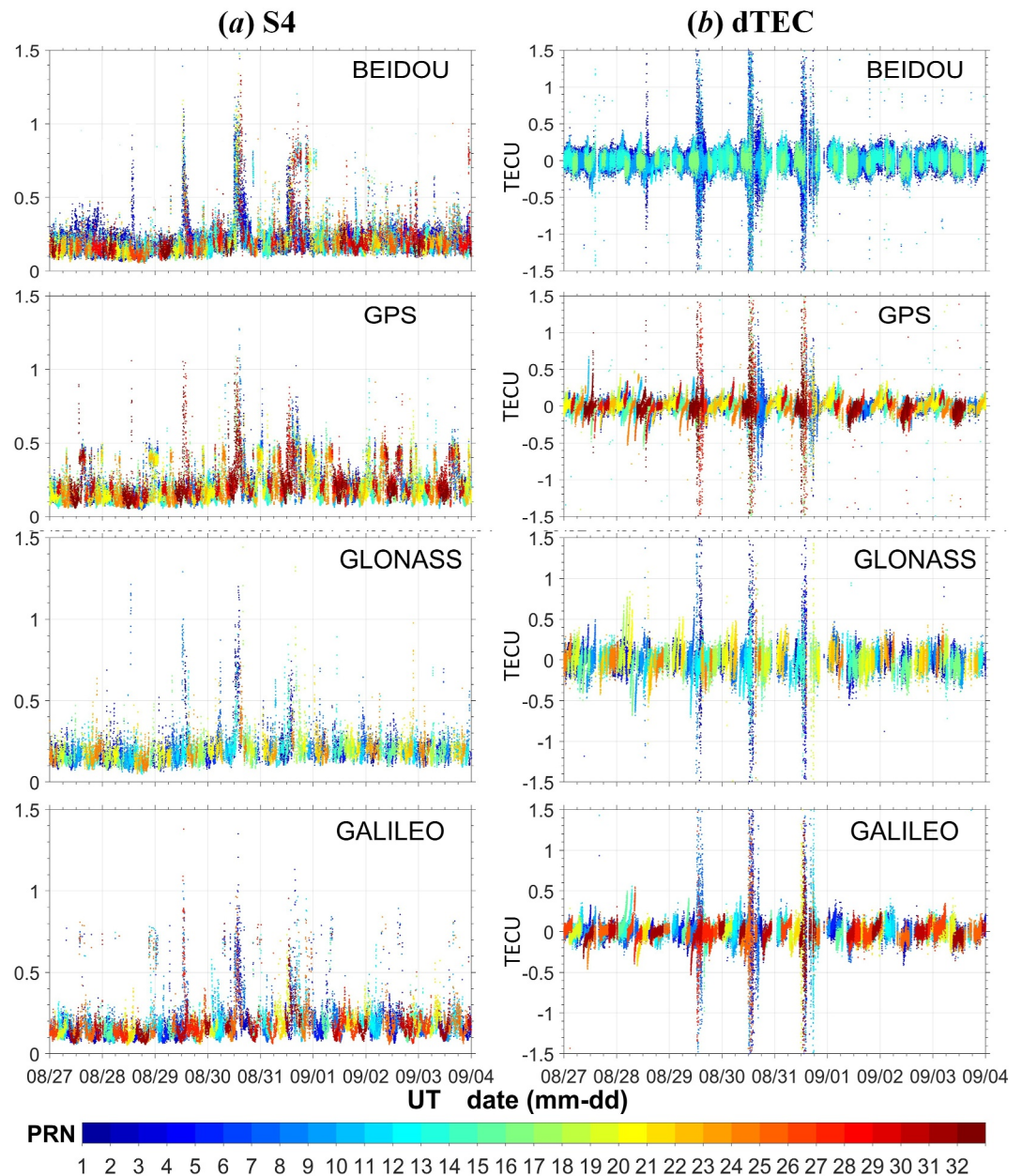


Figure 5. From top to bottom, these are the S4 and dTEC time series for all BeiDou, GPS, GLONASS, and Galileo satellites, spanning from 27 August to 4 September 2023. Subfigure (a) shows S4, which is the ionospheric amplitude scintillation index. Subfigure (b) displays dTEC, which represents rapid TEC changes. The scatter points in various colors represent different satellite numbers within the system, as indicated by the color bar.

3.1.2. Supporting Observations From Ground-Based GNSS Stations

To confirm that the observed phenomena were not coincidental and to investigate the spatial location of ionospheric irregularities, we used data from ground stations of Hong Kong, located in the vicinity of the typhoon. Figure 7 presents the GNSS-derived S4 index from the HKLT station in Hong Kong on August 30, capturing scintillation events across BeiDou, GPS, GLONASS, and Galileo. Significant ionospheric disturbances are observed between 12:00 and 18:00 UT, with S4 values peaking around 1.5 for BeiDou and GPS, and slightly lower for GLONASS and Galileo, reaching about 1.0. The simultaneous occurrence and similar intensity of these scintillation events across all four satellite constellations suggest a widespread ionospheric disturbance, affecting multiple GNSS systems at the same time.

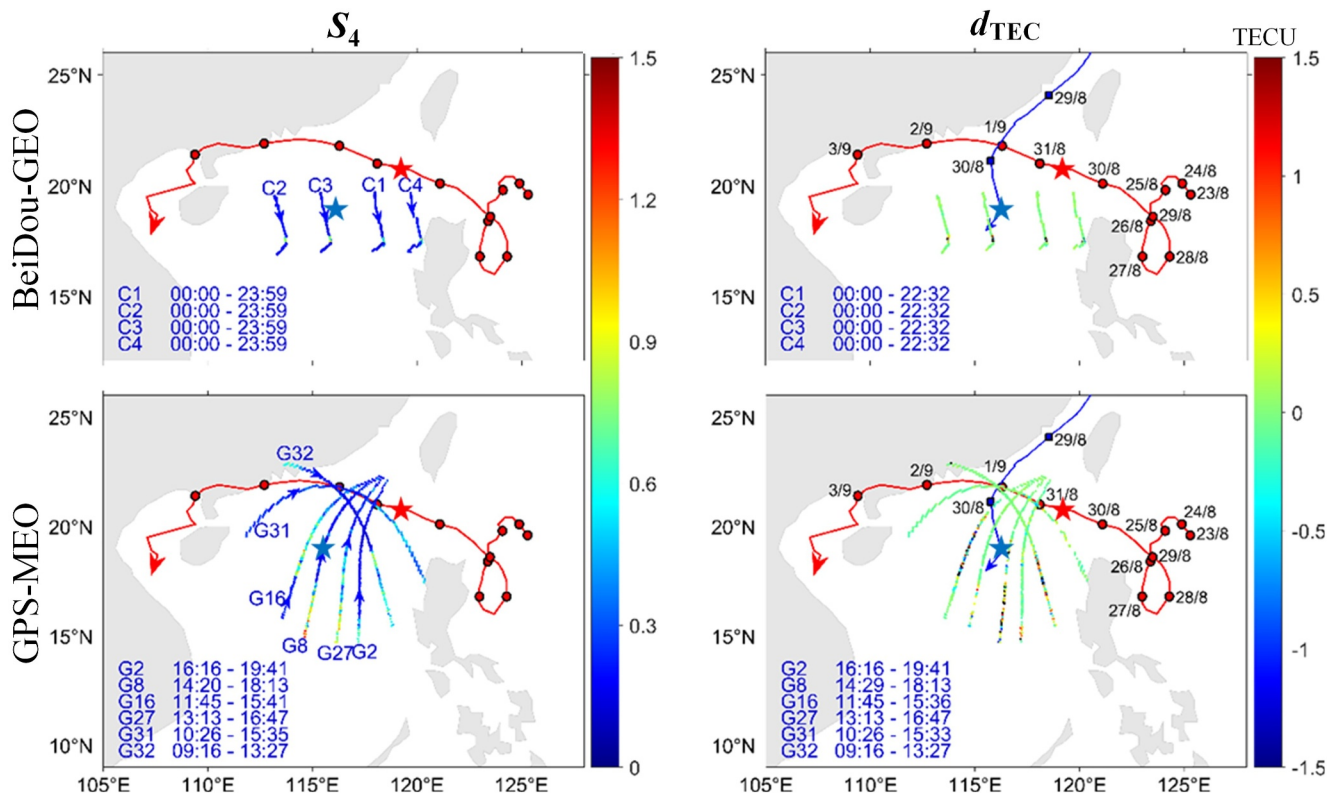


Figure 6. S_4 and $d\text{TEC}$ along the BeiDou-GEO and GPS-MEO satellite IPP trajectories on 30 August 2023. The red trajectory with dots and arrows represents the path of Typhoon Saola, while the blue trajectory with dots and arrows shows the movement of the ship. At the time of scintillation events, the approximate locations of the typhoon and the ship are marked with red and blue stars, respectively. The scatter points indicate the $d\text{TEC}$ values along the IPP, as shown on the color axis. The start and end times of signal reception for each satellite, as recorded by the shipborne ISMR, are noted in the bottom left corner.

It should be noted that this scintillation activity observed between 12:00 and 18:00 UT falls outside the typical time window for Pre-Reversal Enhancement (PRE) (Kumar et al., 2016), which usually occurs between 18:00 and 21:00 LT (local time) for example, around 10:00 to 13:00 UT in low-latitude regions such as Hong Kong. Therefore, it is unlikely that PRE is the primary cause of the scintillations observed in this case. Instead, the strong scintillation is more likely linked to Typhoon Saola, which was active during this period. Typhoons can generate gravity waves that propagate upward, triggering TIDs. These gravity waves could also lead to instabilities in the upper atmosphere, resulting in the widespread and intense scintillation observed across multiple GNSS constellations (Yu et al., 2022).

To further investigate the location of ionospheric irregularities, we plotted the S_4 values and corresponding IPP trajectories for BeiDou, GPS, GLONASS, and Galileo between 12:00 and 24:00 UT, as shown in Figure 8. The scintillation events, indicated by red points, are primarily concentrated between 18°N and 21°N latitude and around 114°E longitude. This distribution closely aligns with the shipborne observations presented in Figure 6, further corroborating the accuracy of both the shipborne measurements and the associated analyses.

3.2. HF Radar Observations to Ionospheric Irregularities

To delve into whether the scintillations observed are attributed to EPB structures, we scrutinized the long-range backscatter echoes captured by the eastward-oriented HF radar of LARID, as illustrated in Figure 9. Notably, a significant proportion of the backscatter echoes, consistently appearing at distances approximately ranging from 2,000 to 3,000 km, exhibited relatively low Doppler velocities (within ± 20 m/s) and spectral widths (less than 20 m/s), thus classified as ground scatter. However, within the range gates spanning 0–1,500 km, robust backscatter echoes were observed, characterized by a substantial increase in data points with significantly higher Doppler velocities (roughly 50–150 m/s) and spectral widths (10–80 m/s) compared to ground scatter. This suggests that these echoes originate from backscatter caused by ionospheric irregularities.

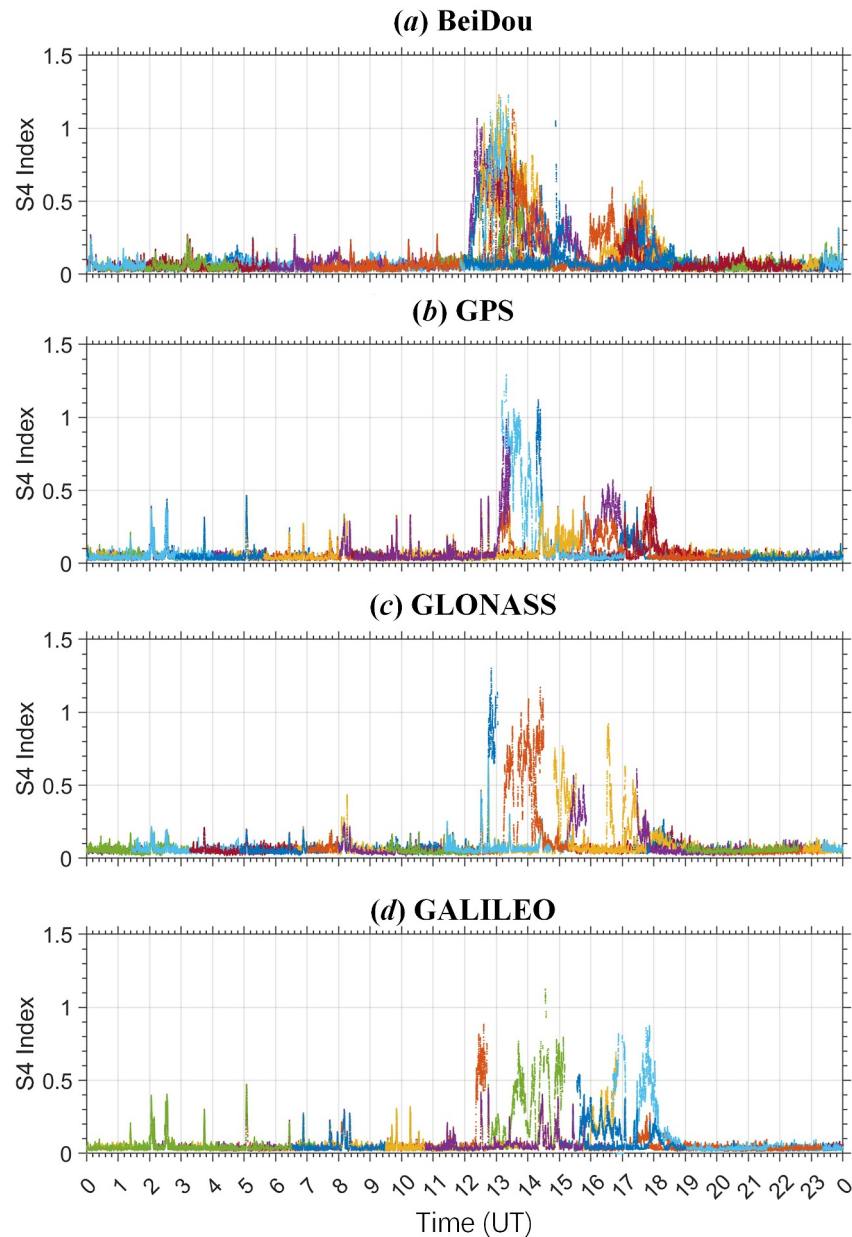


Figure 7. GNSS-derived S4 from HKLT station in Hong Kong on August 30. Subplots (a) to (d) represent BeiDou, GPS, GLONASS, and Galileo, respectively. The x -axis indicates Universal Time, and the y -axis represents the scintillation index. Different colors distinguish between satellites, and the elevation cutoff angle is set to 30° .

Specifically, from 12:00 to 16:00 UT, we can see a continuous emergence and subsequent decay of regions exhibiting backscatter from ionospheric irregularities at distances of 500–1,500 km. These irregular regions were sporadically structured during sunset hours on 28 August, became more prominent on 29 August, reached their peak on 30 August, and gradually dissipated by 1 September. Notably, during their peak on 30 August, these irregularity regions persisted for nearly 6 hours, with an average Doppler velocity of approximately 100 m/s, and displayed more significant fluctuations in spectral width. Concurrently, the higher SNRs, both in intensity and extent, indicated the presence of more conspicuous and extensive irregular structures on this particular day. These observations strongly suggest that the scintillations observed in ionospheric irregularities are likely attributed to EPB structures (Sun et al., 2023).

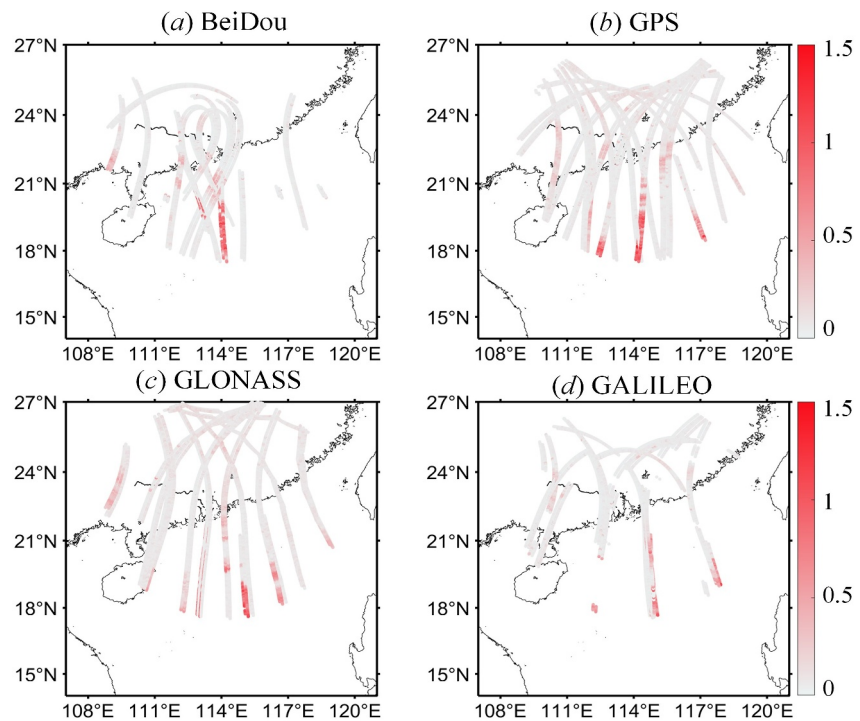


Figure 8. Mapping the IPP trajectories and corresponding S4 values from the HKLT and HKSC stations in Hong Kong on August 30, between 12:00 and 24:00 UT. Subplots (a) to (d) represent BeiDou, GPS, GLONASS, and Galileo, respectively. The color scale ranges from 0 to 1.5, and the elevation cutoff angle is set to 30°.

The irregularity regions observed by the HF radar are temporally and spatially correlated with the activity of TC Saola before and during the sunset-time fluctuations recorded by shipborne ISMR observations. The radar-detected irregularities occurred during sunset hours near the autumnal equinox, lasting between 3 and 6 hr, which is consistent with the temporal patterns of EPBs (Sun et al., 2023; Zou et al., 2024). Similar to the ISMR observations, the radar revealed a progression of nascent irregularity patterns on 28 August, becoming more prominent from 29 to 31 August, peaking on 30 August, and fading after 1 September. This evolution aligns with the intensification of TC Saola, whose westward movement toward the radar on 29 August and subsequent northeastward shift away from the radar by 1 September.

In the aspect of the spatial correlation, the backscattered echoes can be projected onto altitude and geographic longitude at the radar site's latitude (19.2°N) using sine and cosine transformations aided by the radar's fixed elevation angle of 18°. As a result, the irregularities were observed in the ionosphere at altitudes ranging from approximately 150 to 450 km and longitudes spanning from 113.4° to 122.5°E. This matches the tendency of EPBs to form in the F region of the low-latitude ionosphere (Jia et al., 2023; Sun et al., 2021) and meets the influence zone of TC Saola. These indicate that the irregular structures characterized by enhanced S4 and dTEC fluctuations during sunset, as well as the irregular regions detected by HF radar backscatter, are manifestations of the same EPB structures. Moreover, the growth and dissipation of these EPB structures are closely linked to the approach and subsequent departure of TC Saola.

The near disappearance of EPBs on September 1st, despite the typhoon still being present in the South China Sea, can be attributed to several factors related to the interaction between typhoon-induced atmospheric disturbances and ionospheric conditions (Li et al., 2018). Typhoon-generated gravity waves, while often acting as a seed for plasma instabilities, can sometimes suppress the formation of EPBs depending on their phase, strength, and propagation characteristics. This suppression occurs when gravity waves disrupt the development of ionospheric irregularities necessary for EPB formation (Sivakandan et al., 2019). Additionally, the typhoon's influence on upper atmospheric dynamics, particularly through wind shear and zonal wind alterations, can inhibit the vertical plasma drifts crucial for EPB generation (Olawepo et al., 2023; Tsai et al., 2024). The resultant disruption in

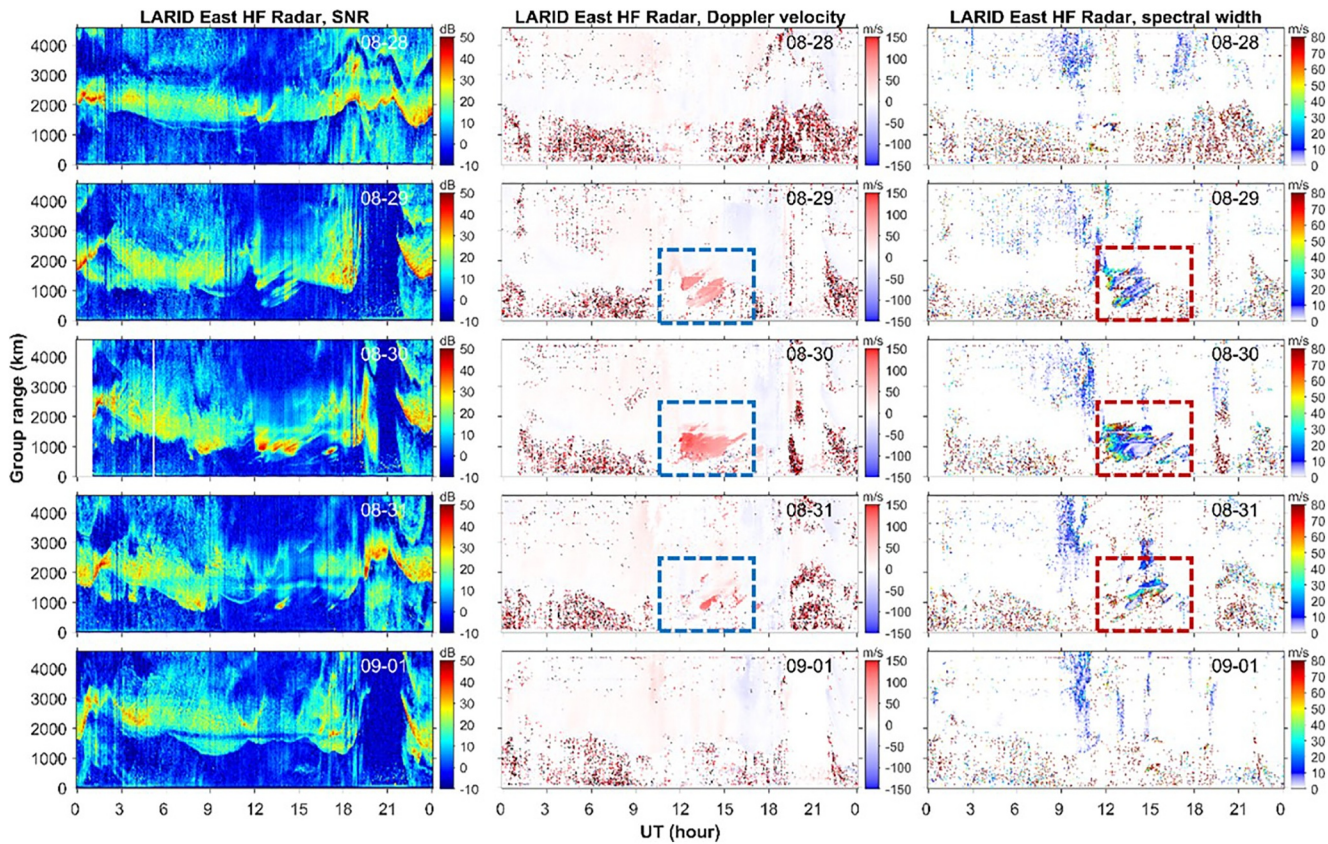


Figure 9. The SNR, Doppler velocity, and echo spectrum bandwidth of the backscattered echo recorded by the LARID east-facing HF radar from 28 August to 1 September 2023. Here, a negative (positive) Doppler velocity indicates that the backscattered object is moving toward (away from) the radar. The horizontal axis represents Universal Time. The left vertical axis signifies the group range in kilometers (km). The colorbar represent SNR in decibels (dB), Doppler velocity in meters per second (m/s), and spectral width, also expressed in meters per second (m/s).

plasma movement may explain the decreased visibility of EPBs on HF radar, even though the typhoon remained active in the region.

It is worth noting that for HF radar, observations can encounter intricate ray paths at low latitudes due to significant modifications in the ionosphere caused by EPBs and other ionospheric irregularities. Consequently, discrepancies may arise between the actual position of the irregular backscattered echo and the aforementioned results. In the case of over-the-horizon radar observations, a wider range gate does not solely indicate a higher altitude; it could also signify a 1.5-hop backscatter echo occurring at a lower altitude (Hu et al., 2024).

3.3. In-Situ Electron Density Variations by SWARM

Data from the Swarm satellite are employed for cross-validation. During the period of TC Saola's activity, the SwarmB satellite passed overhead and recorded stable electron density data. Specifically, from 28 August to 1 September 2023, SwarmB maintained an altitude near 500 km while traversing the South China Sea, residing within the F layer of the ionosphere. The electron density observations from SwarmB offer a direct reflection of ionospheric variations (Jin et al., 2020; Spogli et al., 2023).

As depicted in Figure 10, there is a considerable electron density depletion observed at latitudes between 10°N and 20°N during sunset from 29 to 31 August. Conversely, there was no noticeable loss of electron density observed on the eve of TC Saola's entry into the South China Sea on 28 August or after its landfall on 1 September. The presence of EPBs can be identified by plasma density (electron density) depletions (McClure et al., 1977). Therefore, the electron density depletion observed near the F layer of the ionosphere at an altitude of 500 km aligns with the signature of the large-scale, low-density structure of EPB rising from the base of the F layer. This

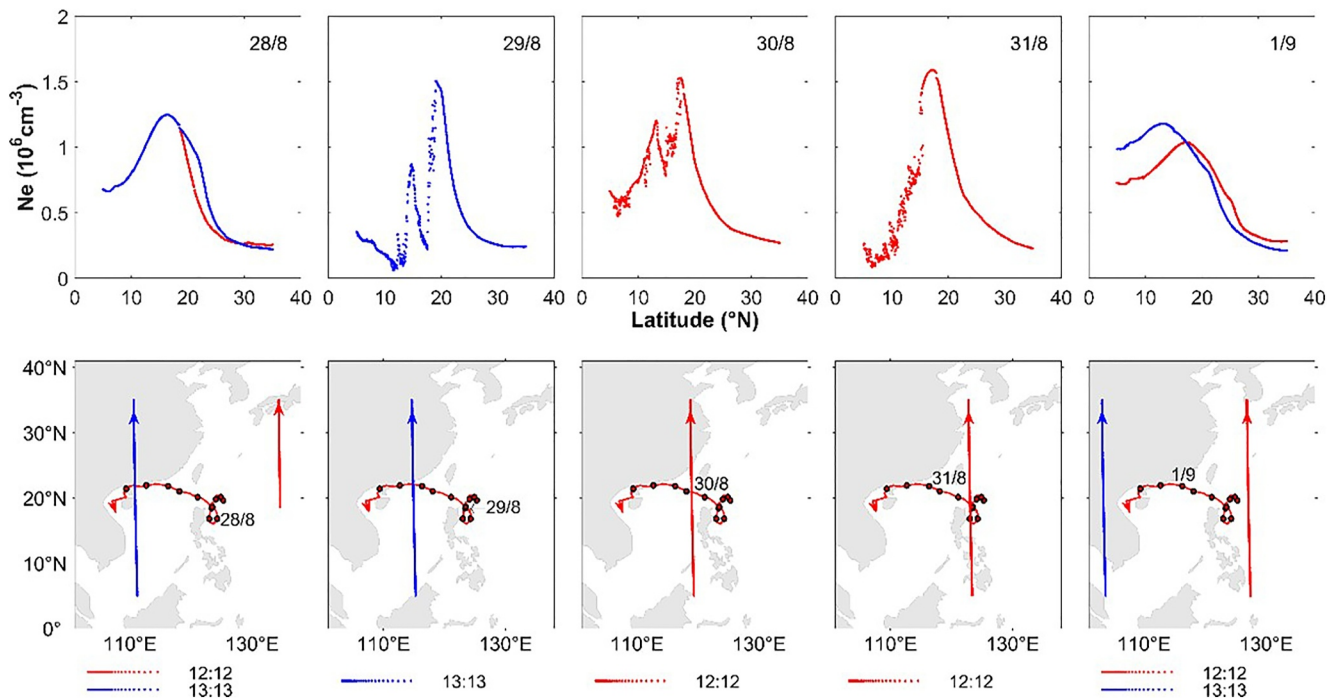


Figure 10. Electron density was detected by the SwarmB satellite during its passage through the South China Sea and adjacent areas between 12:00 and 16:00 UT daily from 28 August to 1 September 2023. In the top set, the horizontal axis represents latitude, and the vertical axis represents electron density (Ne), measured in units of $10^6/\text{cm}^3$, showing the variation of Ne with latitude for each day from left to right. The bottom set depicts the trajectories of the SwarmB satellite and the typhoon for each day. The red scattered points indicate the SwarmB satellite passing by at 12:12 UT, while the blue scattered points represent the SwarmB satellite passing by at 13:13 UT.

implies that the latitude of the electron density depletion structure detected by SwarmB can serve as an indicator of the approximate latitude of the EPB structure.

Furthermore, the intensity and latitudinal movement of the electron density depletion structure at the same time each day can provide insights into the EPB intensity and the potential north-south movement of the overall structure. As shown in Figure 10, at 12:12 UT, the electron density depletion on 30 August was more pronounced compared to 31 August, and it was more concentrated between 13.3°N and 17.0°N . However, on 31 August, the electron density depletion between 10°N and 20°N was significantly weaker, and there were also indications of suspected electron density depletion near 5°N – 10°N . This suggests that the EPB structure may have exhibited signs of overall dissipation toward the south.

4. The Impacts on the Positioning Performance

As one of the prevalent GNSS positioning techniques, precise point positioning (PPP) mode is utilized to investigate the impact of typhoons on positioning accuracy. The detailed parameter settings for GPS dual-frequency PPP are shown in Table 1.

Under normal conditions, the kinematic PPP can achieve decimeter-level accuracy for the receiver with the above processing strategies (Geng et al., 2019; Teunissen, 2020). To assess the impact of typhoons on kinematic PPP precision, we analyzed PPP results obtained during 2 days: 30 August, when the super typhoon reached its peak, and 1 September, when the typhoon dissipated and moved northward. In our case, the PPP errors are compared to a combined solution of PPP and inertial navigation system solution by the Inertial Explorer software.

Figure 11 presents the PPP positioning error results for 30 August, with a particular focus on the occurrence of ionospheric scintillation. The PPP results for the components above X, Y, and Z were at 0.146, 0.254, and 0.055 m, respectively. However, during sunset, a significant increase in positioning error was observed, peaking at 2.785 m. This increase coincided precisely with the enhanced fluctuations in the GPS signal received by the shipboard scintillation receiver, particularly during the sunset hours between 12:00 and 18:00. In comparison,

Table 1
Data Processing Settings for GPS Dual-Frequency PPP

Item	Techniques and implementations
Observations	GPS dual-frequency code and phase measurements
Processing mode	Forward
Sampling interval	30 s
Elevation mask angle	7°
Cycle-slip detection	Phase Geometry-free and Hatch-Melbourne-Wubben combination (Blewitt, 1990)
Satellite orbit	Fixed with the final products from IGS with an interval of 15 min
Satellite clock	Fixed with the final products from IGS with an interval of 5 min
Phase center offset	igs08.atx
Ionospheric delay	IF-model: First-order effect eliminated by ionospheric-free linear combination
Differential Code Bias	Corrected by PIC1 DCBs from Center for Orbit Determination in Europe
Tropospheric delay	The Saastamoinen model for the initial zenith dry and wet delay (Saastamoinen, 1972), along with the GMF projection function (Böhm et al., 2006), and the wet delay is estimated as constant every 2 hr
Solid earth tide, ocean tide loading, and pole tide	IERS Conventions 2010 (Petit & Luzum, 2010); FES2004 (Lyard et al., 2006) for ocean tides
Relativity effect	IERS Conventions 2010

while the PPP results for 1 September exhibited some instability, the magnitude of these variations during sunset was significantly smaller than those observed on 30 August.

Typically, the degradation of PPP is caused by plasma bubbles during the post-sunset period at low latitudes. However, on August 30, the degradation of shipborne GPS-based PPP occurred prior to sunset. As shown in Figure 5, between 12:30 and 16:00, four GPS satellites were affected by scintillation. During these scintillation periods, frequent carrier phase cycle slips were observed, reducing the number of satellites available for adjustment. This decrease in redundancy led to an increase in positioning error, exceeding 2 m. In contrast, during the sunset period, scintillation affected only two satellites, resulting in a smaller PPP error of approximately 0.4 m. While plasma bubbles frequently occur during active ionospheric years at low latitudes, they are primarily observed after sunset. Scintillation before sunset is rare, suggesting that the scintillation observed on 30 August may have been caused by typhoon-induced TIDs or irregularities, leading to the deterioration of PPP performance.

It is worth mentioning that even during periods where PPP was able to converge, the achieved accuracy was far from the centimeter-level standard. Although the ionosphere-free combination helped mitigate the first-order ionospheric effects, the combined effects of cycle slips, signal loss, and enhanced tropospheric errors during typhoon conditions prevented PPP from achieving its usual level of performance.

5. Discussion

The observations mentioned above reveal distinct occurrences of EPBs in the South China Sea during the sunset hours from 29 to 31 August 2023. The HF radar and SwarmB data suggest that the potential impact zone of these EPBs extended broadly from longitudes 113.4°E to 122.5°E and latitudes 10°N to 20°N. Notably, the center of this potential impact zone is centered at 15°N, 118°E, hinting that the EPBs may have originated from the eastern flank of the South China Sea. This coincides well with the location of station S4 and the fluctuations in dTEC recorded by the shipborne ISMR. During this period, Typhoon Saola moved from east to west across the South China Sea originating from its eastern region. It is noteworthy that during our study period from 28 August to 1 September 2023, geomagnetic activity remained relatively stable in comparison to solar activity. Given the temporal concurrence of TC Saola's passage with the emergence of EPBs, it is plausible that the typhoon's activity, rather than geomagnetic activity, played a significant role in the formation of these EPB structures. Specifically, as TC Saola entered the South China Sea, the intensity of the EPBs was observed to increase notably.

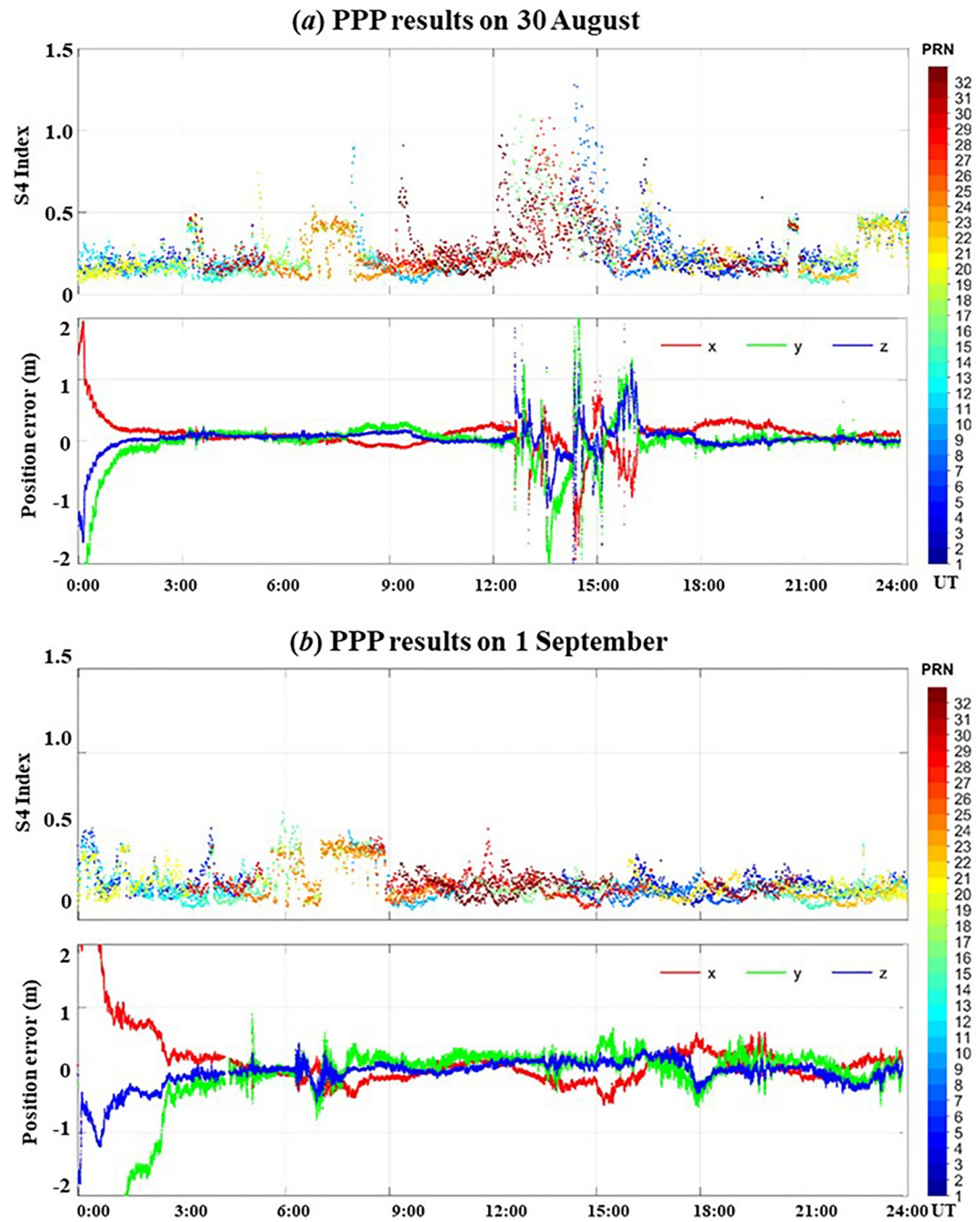


Figure 11. Subplots (a) and (b) illustrate the PPP performance for shipborne receiver with S4 on 30 August and 1 September 2023, respectively. In each subplot, the upper graph represents S4, with scattered points of different colors showing GPS satellites from 1 to 32, as indicated by the color bar; the vertical axis depicts the degree of scintillation. The lower graph in each subplot displays PPP positioning results in the x , y , and z directions, with red representing x , green representing y , and blue representing z ; the horizontal axis represents Universal Time; the vertical axis represents positioning errors in meters.

Further, the mechanisms of EPB generation, atmospheric wave, and the analysis in combined with observations in this study are analyzed as follows:

Generally, EPBs in low latitudes are primarily attributed to the Rayleigh-Taylor (R-T) instability mechanism (Kelley, 2009; Makela & Otsuka, 2012), which is influenced by several factors, including zonal electric fields and neutral winds (Abdu, 2001). Studies have shown that the initial seed of unstable density disturbances is gravity

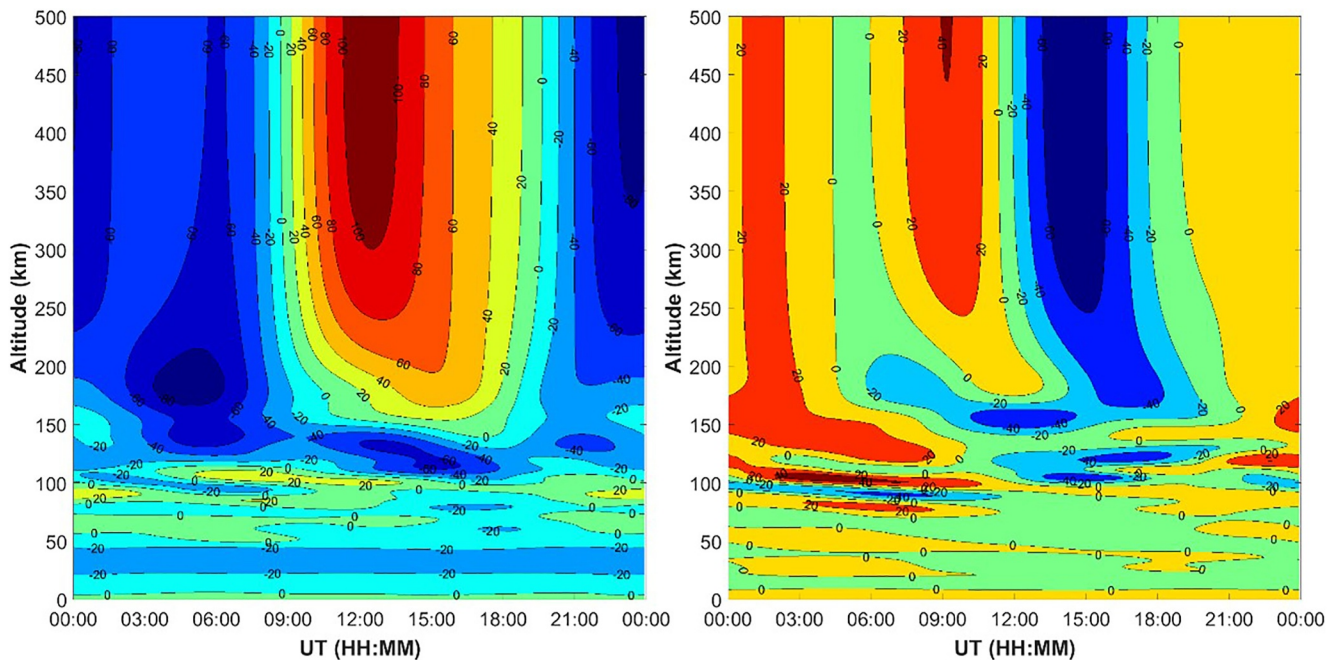


Figure 12. The temporal variation of zonal (left subplots with eastward winds denoted as positive, mark in red) and meridional (right, with northward winds denoted as positive, mark in red) wind components in the 2014 Horizontal Wind Model (HWM14) spanning altitudes from 0 to 500 km on 30 August 2023. The horizontal axis represents Universal Time, while the vertical axis represents altitude.

waves (Huang & Kelley, 1996; Singh et al., 1997; H Takahashi et al., 2009). Gravity waves generated by mesoscale convective systems within the Intertropical Convergence Zone (ITCZ) can trigger dispersion mechanisms, thereby facilitating the development of EPBs (Tsunoda, 2010a, 2010b). This finding is further supported by recent studies (Aa et al., 2022; Barad et al., 2024; Ghodpage et al., 2024; Takahashi et al., 2020).

The background neutral winds play a pivotal role in mediating the interaction between gravity waves and EPBs. As early as 1960, it was observed that the propagation characteristics of ascending gravity waves might be influenced by background winds (Hines, 1960). Subsequent research has revealed that different directions of background winds can lead to varying modes of gravity wave propagation (Cowling et al., 1971). Gravity waves traveling against the background wind are more likely to reach the ionosphere due to less wave dissipation compared to those moving with the wind (Waldock & Jones, 1984). These findings provide a theoretical framework for understanding the potential connection between typhoons and EPB phenomena (Mao et al., 2010).

Thus, it is crucial to examine the background winds. On 30 August 2023, at 12:00 UT, the cyclone center of TC Saola was positioned at 20.7°N, 119.7°E, a location closest to the speculated EPB generation point. During this time, intense responses were observed from shipborne ISMR, ground GNSS stations, an eastward-looking HF radar, and SwarmB. Figure 12 depicts the diurnal variation of zonal and meridional winds spanning altitudes from 0 to 500 km, utilizing the empirical Horizontal Wind Model 2014 (HWM14) (Drob et al., 2015).

The zonal wind chart shows that after sunset on August 30, a broad region of slow, westward winds dominated the upper ionosphere from 12:00 to 18:00 UT. These winds extended from the potential typhoon height around 15 km up to the more concentrated ionospheric altitudes at approximately 75 km. Notably, between 100 and 150 km, there was a strong westward wind, which gradually shifted to a strong eastward wind above 150 km. Similarly, the meridional wind chart indicates that from 12:00 to 18:00 UT, winds below 100 km were relatively weak, while winds above 100 km were predominantly southward. Overall, the upper atmosphere was characterized by a southwestward wind direction.

Meanwhile, on August 30 before sunset, Typhoon Saola moved predominantly from east to west and south to north, near 119°E, 20°N, northeast of the observed ionospheric irregularities, located approximately between

113°E to 120°E and 15°N to 20°N. Gravity waves typically propagate against the background wind (Li et al., 2022; Vadas, 2007), which implies that the observed irregularities were unlikely to be directly caused by gravity waves originating from the typhoon's center. However, Typhoon Saola's radius of gale-force winds (220–250 km) and the strong convection occurring several hundred kilometers from the typhoon's center could have generated atmospheric disturbances encompassing the region beneath the observed ionospheric irregularities. These disturbances may have propagated upward into the middle and upper atmosphere, where they engaged in coupling mechanisms with the ionosphere, potentially leading to EPB formation.

From the above observations and discussions, the mechanism of the observed EPBs during Typhoon Saola can be explained as follows. The intense convection associated with the typhoon continuously generated AGWs, as compressed air near the typhoon center was lifted by adjacent rising air, propagating obliquely upwards. Before sunset, these gravity waves, driven by background winds, penetrated the top of the troposphere and reached the ionosphere. As they ascended, the waves may have undergone breaking or attenuation processes (Vadas & Liu, 2009). Initial density perturbations at the bottom of the F-layer then propagated upward, causing wave-like disturbances in plasma density through neutral-charged particle interactions, ultimately triggering plasma instabilities and forming EPBs in low-latitude regions. These prominent EPB structures in the F-layer disrupted trans-ionospheric radio signals, as detected by HF radars and Swarm satellites, severely impacting navigation systems.

6. Conclusions

A multifaceted approach was undertaken to investigate the ionospheric irregularities that coincided with Tropical Cyclone Saola during the crucial period from 29 to 31 August 2023. This examination integrated data from ship-borne ISMRs, ground GNSS stations, the LARID HF radar, and the Swarm satellite.

Firstly, this finding highlights the exceptional ability of ship-borne ISMRs to identify the characteristic signatures of EPBs at low latitudes. These signatures are prominently manifested in fluctuations of the S4 index and dTEC. When combined with HF radar and Swarm satellite data, we have demarcated a potential impact area for EPB stretching across the South China Sea, spanning latitudes 10°N to 20°N and longitudes 113.4°E to 122.5°E, during the sunset hours of the specified dates.

Secondly, we emphasize the significant potential for these ionospheric irregularities to disrupt satellite navigation signals, particularly impacting the precision of PPP. Even when PPP achieves convergence to sub-decimeter levels, the presence of EPBs can abruptly disrupt this convergence, causing positioning accuracy to degrade to meter-scale levels. This underscores the detrimental effects of EPBs on navigation systems.

Finally, this research suggests that the proximity of Tropical Cyclone Saola to the South China Sea may have influenced the observed ionospheric irregularities prior to the pre-reversal enhancement, possibly through atmospheric waves. The temporal and spatial alignment between these irregularities and the typhoon's trajectory indicates a potential, albeit tentative, causal link. We hypothesize that the interaction between background winds and the typhoon may have facilitated gravity wave propagation, potentially affecting the upper atmosphere-ionosphere coupling and possibly contributing to the formation of EPBs.

Data Availability Statement

The IMF data are provided from CDAWeb at <https://cdaweb.sci.gsfc.nasa.gov/>. The F10.7 and Dst index are provided by the Goddard Space Flight Center (GSFC) from <https://omniweb.gsfc.nasa.gov/>. The ISMR data obtained during the shipborne experiment is available upon request by contacting the author. The LARID data can be accessed offline at Beijing National Observatory of Space Environment, Institute of Geology and Geophysics Chinese Academy of Sciences or online through the Geophysics center, National Earth System Science Data Center (<http://wdc.geophys.ac.cn>). The publicly available Swarm data is provided by the European Space Agency (ESA), accessible through their portal: <https://earth.esa.int/eogateway/missions/swarm/data>. The GNSS station raw observation data of the Hong Kong GNSS network (SatRef) are publicly available for download at: https://www.geodetic.gov.hk/sc/satref/RINEX_download.htm. The RTKLIB package (version 2.4.3 b34) for the positioning performances could be download at <http://www.rtklib.com/>.

Acknowledgments

The study is funded by National Natural Science Foundation of China (42004012), Natural Science Foundation of Shandong Province, China (ZR2024MD094, ZR2022MD034), the Young Scholars Program of Shandong University, Weihai and Youth Innovation Team Development Project of Higher School in Shandong Province (2023KJ143), the International Partnership Program of Chinese Academy of Sciences (183311KYSB20200003), Xiaomi Young Talents Program, the Chinese Meridian Project, and the National Key Laboratory of Electromagnetic Environment (JCKY2022210C614240301). The authors are grateful for the use of the LARID data, which were from the IONISE project supported by the National Natural Science Foundation of China (42020104002) and the Solar-Terrestrial Environment Research Network (STERN) of Chinese Academy of Sciences, and We appreciate the discussion on the typhoon related EPB generation mechanism with Dr. Wenjie Sun from Key Laboratory of Earth and Planetary Physics, Institute of Geology and Geophysics, Chinese Academy of Sciences, Beijing, China.

References

- Aa, E., Zhang, S. R., Erickson, P. J., Vierinen, J., Coster, A. J., Goncharenko, L. P., et al. (2022). Significant ionospheric hole and equatorial plasma bubbles after the 2022 Tonga volcano eruption. *Space Weather*, 20(7), e2022SW003101. <https://doi.org/10.1029/2022sw003101>
- Abdu, M. A. (2001). Outstanding problems in the equatorial ionosphere–thermosphere electrodynamics relevant to spread F. *Journal of Atmospheric and Solar-Terrestrial Physics*, 63(9), 869–884. [https://doi.org/10.1016/s1364-6826\(00\)00201-7](https://doi.org/10.1016/s1364-6826(00)00201-7)
- Ajith, K., Li, G., Tulasi Ram, S., Yamamoto, M., Hozumi, K., Abadi, P., & Xie, H. (2020). On the seeding of periodic equatorial plasma bubbles by gravity waves associated with tropical cyclone: A case study. *Journal of Geophysical Research: Space Physics*, 125(10), e2020JA028003. <https://doi.org/10.1029/2020ja028003>
- Anthes, R. A. (1974). The dynamics and energetics of mature tropical cyclones. *Reviews of Geophysics*, 12(3), 495–522. <https://doi.org/10.1029/rg012i003p00495>
- Barad, R. K., Sripathi, S., Banola, S., & Vijaykumar, K. (2024). Occurrence of equatorial plasma bubbles (EPBs) over the Indian region on 15 January 2022 and their plausible connection to the Tonga volcano eruption. *Journal of Geophysical Research: Space Physics*, 129(6), e2023JA031542. <https://doi.org/10.1029/2023ja031542>
- Bauer, S. J. (1958). An apparent ionospheric response to the passage of hurricanes. *Journal of Geophysical Research*, 63(1), 265–269. <https://doi.org/10.1029/jz063i001p00265>
- Bennett, C. L. (2023). A novel population of slow magnetosonic waves and a method for the observation of the roots of plasma bubbles in the lower ionosphere. *Journal of Geophysical Research: Space Physics*, 128(5), e2022JA030855. <https://doi.org/10.1029/2022ja030855>
- Blewitt, G. (1990). An automatic editing algorithm for GPS data. *Geophysical Research Letters*, 17(3), 199–202. <https://doi.org/10.1029/g1017i003p00199>
- Böhm, J., Niell, A., Schuh, H., Tesmer, V., & Tregoning, P. (2006). Mapping functions for atmospheric delay modelling in GNSS analysis: Na. Chen, J., Zhang, X., Ren, X., Zhang, J., Freeshah, M., & Zhao, Z. (2020). Ionospheric disturbances detected during a typhoon based on GNSS phase observations: A case study for typhoon Mangkhut over Hong Kong. *Advances in Space Research*, 66(7), 1743–1753. <https://doi.org/10.1016/j.asr.2020.06.006>
- Chen, P., Xiong, M., Yao, Y., Chen, H., Tang, F., Qiu, L., & Zhang, Y. (2024). On the ionospheric response in the Taiwan region to typhoon Meranti in September 2016. *Geodesy and Geodynamics*. <https://doi.org/10.1016/j.geog.2024.05.003>
- Chernogor, L., & Frolov, V. (2013). Features of propagation of the acoustic-gravity waves generated by high-power periodic radiation. *Radiophysics and Quantum Electronics*, 56(4), 197–215. <https://doi.org/10.1007/s11141-013-9426-0>
- Chernogor, L. F., Garmash, K. P., Guo, Q., Rozumenko, V. T., Zheng, Y., & Luo, Y. (2022). Disturbances in the ionosphere that accompanied typhoon activity in the vicinity of China in September 2019. *Radio Science*, 57(4), 1–24. <https://doi.org/10.1029/2022rs007431>
- Chou, M. Y., Lin, C. C., Yue, J., Tsai, H. F., Sun, Y. Y., Liu, J. Y., & Chen, C. H. (2017). Concentric traveling ionosphere disturbances triggered by Super Typhoon Meranti (2016). *Geophysical Research Letters*, 44(3), 1219–1226. <https://doi.org/10.1002/2016gl072205>
- Cowling, D., Webb, H., & Yeh, K. (1971). Group rays of internal gravity waves in a wind-stratified atmosphere. *Journal of Geophysical Research*, 76(1), 213–220. <https://doi.org/10.1029/ja076i001p00213>
- De Michelis, P., Consolini, G., Pignatelli, A., Lovati, G., Pezzopane, M., Tozzi, R., et al. (2022). Ionospheric turbulence: A challenge for GPS loss of lock understanding. *Space Weather*, 20(7), e2022SW003129. <https://doi.org/10.1029/2022sw003129>
- Drob, D. P., Emmert, J. T., Meriwether, J. W., Makela, J. J., Doornbos, E., Conde, M., et al. (2015). An update to the Horizontal Wind Model (HWM): The quiet time thermosphere. *Earth and Space Science*, 2(7), 301–319. <https://doi.org/10.1002/2014ea000089>
- Du, X., Zhou, C., Xu, X., Dong, L., Zhang, X., Wang, Z., & Liu, J. (2023). Statistical relationship of ionospheric disturbances caused by typhoon extinction on the sea. *Journal of Geophysical Research: Space Physics*, 128(11), e2023JA031706. <https://doi.org/10.1029/2023ja031706>
- Fu, J., & Jin, S. (2023). Characterization of ionospheric disturbances following multiple typhoons using GPS-derived TEC. *Journal of Geophysical Research: Space Physics*, 128(1), e2022JA030457. <https://doi.org/10.1029/2022ja030457>
- Geng, J., Guo, J., Chang, H., & Li, X. (2019). Toward global instantaneous decimeter-level positioning using tightly coupled multi-constellation and multi-frequency GNSS. *Journal of Geodesy*, 93(7), 977–991. <https://doi.org/10.1007/s00190-018-1219-y>
- Ghodpage, R., Taori, A., Patil, M., Gurav, O., Patil, R., & Sripathi, S. (2024). Equatorial plasma bubble association with lower atmospheric gravity waves—Further evidences. *Advances in Space Research*, 73(7), 3486–3493. <https://doi.org/10.1016/j.asr.2023.05.056>
- Han, H., Zhong, J., Hao, Y., Wang, N., Wan, X., Huang, F., et al. (2024). Effects of equatorial plasma bubbles on multi-GNSS signals: A case study over south China. *Remote Sensing*, 16(8), 1358. <https://doi.org/10.3390/rs16081358>
- Hines, C. O. (1960). Internal atmospheric gravity waves at ionospheric heights. *Canadian Journal of Physics*, 38(11), 1441–1481. <https://doi.org/10.1139/p60-150>
- Hu, L., Li, G., Ning, B., Sun, W., Xie, H., Zhao, X., et al. (2024). Development of low latitude long range ionospheric radar for observing plasma bubble irregularities and preliminary results. *Journal of Geophysical Research: Space Physics*, 129(3), e2023JA032099. <https://doi.org/10.1029/2023ja032099>
- Huang, C. S., & Kelley, M. C. (1996). Nonlinear evolution of equatorial spread F: I. On the role of plasma instabilities and spatial resonance associated with gravity wave seeding. *Journal of Geophysical Research*, 101(A1), 283–292. <https://doi.org/10.1029/95ja02211>
- Huang, Y. N., Cheng, K., & Chen, S. W. (1985). On the detection of acoustic-gravity waves generated by typhoon by use of real time HF Doppler frequency shift sounding system. *Radio Science*, 20(4), 897–906. <https://doi.org/10.1029/rs020i004p00897>
- Hung, R., & Kuo, J. (1978). Ionospheric observation of gravity-waves associated with hurricane Eloise. *Journal of Geophysics*, 45(1), 67–80.
- Hung, R., Tsao, Y., Lee, C., Johnson, D., Chen, A., Lin, C., & Pan, J. (1990). Observations on thermospheric and mesospheric density disturbances caused by typhoons and convective storms. *Journal of Spacecraft and Rockets*, 27(3), 285–298. <https://doi.org/10.2514/3.26138>
- Hysell, D., Jafari, R., Fritts, D., & Laughman, B. (2014). Gravity wave effects on postsunset equatorial F region stability. *Journal of Geophysical Research: Space Physics*, 119(7), 5847–5860. <https://doi.org/10.1002/2014ja019990>
- Jia, W., Chen, G., Xu, J., Yan, C., Wu, K., Zhang, S., et al. (2023). Observations on the variations of the field-Aligned irregularities in the plasma bubbles at low-latitudes of China. *Journal of Geophysical Research: Space Physics*, 128(11), e2023JA031890. <https://doi.org/10.1029/2023ja031890>
- Jin, Y., Xiong, C., Clausen, L., Spicher, A., Kotova, D., Brask, S., et al. (2020). Ionospheric plasma irregularities based on in situ measurements from the Swarm satellites. *Journal of Geophysical Research: Space Physics*, 125(7), e2020JA028103. <https://doi.org/10.1029/2020ja028103>
- Ke, F., Qi, X., Wang, Y., & Liu, X. (2020). Statistics of ionospheric responses to Southeast Asia's typhoons during 2006–2018 using the rate of change in the TEC index. *Advances in Space Research*, 66(7), 1724–1742. <https://doi.org/10.1016/j.asr.2020.06.003>
- Kelley, M. C. (2009). *The Earth's ionosphere: Plasma physics and electrodynamics*. Academic press.

- Kherani, E. A., Abdu, M. A., De Paula, E., Fritts, D., Sobral, J. H. A., & De Meneses, J. F. (2009). The impact of gravity waves rising from convection in the lower atmosphere on the generation and nonlinear evolution of equatorial bubble. *Ann. Geophys.*, 27(4), 1657–1668. <https://doi.org/10.5194/angeo-27-1657-2009>
- Klobuchar, J. A. (1987). Ionospheric time-delay algorithm for single-frequency GPS users. *IEEE Transactions on Aerospace and Electronic Systems*, AES-23(3), 325–331. <https://doi.org/10.1109/taes.1987.310829>
- Kong, J., Yao, Y., Xu, Y., Kuo, C., Zhang, L., Liu, L., & Zhai, C. (2017). A clear link connecting the troposphere and ionosphere: Ionospheric responses to the 2015 Typhoon Dujuan. *Journal of Geodesy*, 91(9), 1087–1097. <https://doi.org/10.1007/s00190-017-1011-4>
- Kumar, S., Chen, W., Liu, Z., & Ji, S. (2016). Effects of solar and geomagnetic activity on the occurrence of equatorial plasma bubbles over Hong Kong. *Journal of Geophysical Research: Space Physics*, 121(9), 9164–9178. <https://doi.org/10.1002/2016ja022873>
- Li, K., Zhang, D., Zeng, Y., Tian, Y., Dai, G., Liu, Z., et al. (2024). Revisiting the ionospheric disturbances over low latitude region of China during super typhoon Hato. *Space Weather*, 22(5), e2023SW003694. <https://doi.org/10.1029/2023sw003694>
- Li, Q., Xu, J., Liu, H., Liu, X., & Yuan, W. (2022). How do gravity waves triggered by a typhoon propagate from the troposphere to the upper atmosphere? *Atmospheric Chemistry and Physics*, 22(18), 12077–12091. <https://doi.org/10.5194/acp-22-12077-2022>
- Li, W., Yue, J., Wu, S., Yang, Y., Li, Z., Bi, J., & Zhang, K. (2018). Ionospheric responses to typhoons in Australia during 2005–2014 using GNSS and FORMOSAT-3/COSMIC measurements. *GPS Solutions*, 22(3), 1–11. <https://doi.org/10.1007/s10291-018-0722-1>
- Liu, Y.-M., Wang, J.-S., & Suo, Y.-C. (2006). Effects of typhoon on the ionosphere. In *Advances in Geosciences: Volume 2: Solar Terrestrial (ST)* (pp. 351–360). World Scientific.
- Lovati, G., De Michelis, P., Consolini, G., Pezzopane, M., Pignalberi, A., & Berrilli, F. (2023). GPS loss of lock events and their dependence on the Interplanetary magnetic field Orientation. *Journal of Geophysical Research: Space Physics*, 128(7), e2023JA031411. <https://doi.org/10.1029/2023ja031411>
- Lyard, F., Lefevre, F., Letellier, T., & Francis, O. (2006). Modelling the global ocean tides: Modern insights from FES2004. *Ocean Dynamics*, 56(5–6), 394–415. <https://doi.org/10.1007/s10236-006-0086-x>
- Ma, M., Jin, S., & Jin, X. T. (2024). Characteristics of ionospheric disturbances during the 2021 Typhoon Chanthu based on GPS and GLONASS. *Advances in Space Research*, 74(1), 271–283. <https://doi.org/10.1016/j.asr.2024.03.060>
- Makela, J. J., & Otsuka, Y. (2012). Overview of nighttime ionospheric instabilities at low- and mid-latitudes: Coupling aspects resulting in structuring at the mesoscale. *Space Science Reviews*, 168(1–4), 419–440. <https://doi.org/10.1007/s11214-011-9816-6>
- Mao, T., Wang, J., Yang, G., Yu, T., Ping, J., & Suo, Y. (2010). Effects of typhoon Matsa on ionospheric TEC. *Chinese Science Bulletin*, 55(8), 712–717. <https://doi.org/10.1007/s11434-009-0472-0>
- McClure, J., Hanson, W., & Hoffman, J. (1977). Plasma bubbles and irregularities in the equatorial ionosphere. *Journal of Geophysical Research*, 82(19), 2650–2656. <https://doi.org/10.1029/ja082i019p02650>
- Mohandesi, A., Knudsen, D. J., Skone, S., Langley, R. B., & Yau, A. W. (2023). Regional mapping of small-scale equatorial ionospheric irregularities using swarm echo satellite measurements. *Space Weather*, 21(6), e2023SW003417. <https://doi.org/10.1029/2023sw003417>
- Olawepo, A. O., Emmanuel, O. O., Daniel, O., Babatunde, R. A., Kazuo, S., De La Cruz Cueva, R. Y., & Ajani, O. V. (2023). Investigation of the possible dependence of equatorial plasma bubble with travelling ionospheric disturbances using airglow-imager at Abuja. *Advances in Space Research*, 72(10), 4435–4448. <https://doi.org/10.1016/j.asr.2023.08.051>
- Palacios, J., Guerrero, A., Cid, C., Saiz, E., & Cerrato, Y. (2018). Defining scale thresholds for geomagnetic storms through statistics. *Natural Hazards and Earth system sciences discussions*, 2018, 1–17.
- Peng, Y., Scales, W. A., Hartinger, M. D., Xu, Z., & Coyle, S. (2021). Characterization of multi-scale ionospheric irregularities using ground-based and space-based GNSS observations. *Satellite Navigation*, 2(1), 14. <https://doi.org/10.1186/s43020-021-00047-x>
- Petit, G., & Luzum, B. (2010). IERS conventions. *IERS technical note*, 36(1), 2010.
- Rather, M. R., Bhat, A. H., Ramkumar, T., & Malik, M. A. (2024). Exploring the link between convectively generated gravity waves and ionospheric anomalies: Insights from observations near the low-mid latitude geomagnetic transition region. *Advances in Space Research*, 74(2), 1039–1055. <https://doi.org/10.1016/j.asr.2024.04.027>
- Saastamoinen, J. (1972). Atmospheric correction for the troposphere and stratosphere in radio ranging satellites. *The use of artificial satellites for geodesy*, 15, 247–251. <https://doi.org/10.1029/gm015p0247>
- Singh, S., Johnson, F., & Power, R. (1997). Gravity wave seeding of equatorial plasma bubbles. *Journal of Geophysical Research*, 102(A4), 7399–7410. <https://doi.org/10.1029/96ja03998>
- Sivakandan, M., Paulino, I., Ramkumar, T. K., Taori, A., Patra, A. K., Sripathi, S., et al. (2019). Multi-instrument investigation of troposphere-ionosphere coupling and the role of gravity waves in the formation of equatorial plasma bubble. *Journal of Atmospheric and Solar-Terrestrial Physics*, 189, 65–79. <https://doi.org/10.1016/j.jastp.2019.04.006>
- Song, Q., Ding, F., Zhang, X., & Mao, T. (2017). GPS detection of the ionospheric disturbances over China due to impacts of Typhoons Rammasum and Matmo. *Journal of Geophysical Research: Space Physics*, 122(1), 1055–1063. <https://doi.org/10.1002/2016ja023449>
- Spogli, L., Alfonsi, L., & Cesaroni, C. (2023). Stepping into an equatorial plasma bubble with a Swarm overfly. *Space Weather*, 21(5), e2022SW003331. <https://doi.org/10.1029/2022sw003331>
- Sun, L., Xu, J., Wang, W., Yuan, W., Li, Q., & Jiang, C. (2016). A statistical analysis of equatorial plasma bubble structures based on an all-sky airglow imager network in China. *Journal of Geophysical Research: Space Physics*, 121(11), 11495–11517. <https://doi.org/10.1002/2016ja022950>
- Sun, L., Xu, J., Zhu, Y., Yuan, W., Gao, H., & Yan, C. (2023). Multi-source perturbations in the evolution of a low-latitude equatorial plasma bubble event occurred over China. *Space Weather*, 21(3), e2022SW003293. <https://doi.org/10.1029/2022sw003293>
- Sun, L., Xu, J., Zhu, Y., Yuan, W., & Zhao, X. (2021). Case study of an Equatorial Plasma Bubble Event investigated by multiple ground-based instruments at low latitudes over China. *Earth and Planetary Physics*, 5(5), 435–449. <https://doi.org/10.26464/epp2021048>
- Sun, W., Li, G., Zhang, S. R., Hu, L., Dai, G., Zhao, B., et al. (2024). Regional ionospheric super bubble induced by significant upward plasma drift during the 1 December 2023 geomagnetic storm. *Journal of Geophysical Research: Space Physics*, 129(6), e2024JA032430. <https://doi.org/10.1029/2024ja032430>
- Takahashi, H., Taylor, M. J., Pautet, P.-D., Medeiros, A., Gobbi, D., Wrasse, C., et al. (2009). Simultaneous observation of ionospheric plasma bubbles and mesospheric gravity waves during the SpreadFEx Campaign. *Paper presented at the Annales Geophysicae*. <https://doi.org/10.5194/angeo-27-1477-2009>
- Takahashi, H., Wrasse, C. M., Figueiredo, C. A. O. B., Barros, D., Paulino, I., Essien, P., et al. (2020). Equatorial plasma bubble occurrence under propagation of MSTID and MLT gravity waves. *Journal of Geophysical Research: Space Physics*, 125(9), e2019JA027566. <https://doi.org/10.1029/2019ja027566>
- Taylor, M. J., Jahn, J. M., Fukao, S., & Saito, A. (1998). Possible evidence of gravity wave coupling into the mid-latitude F region ionosphere during the SEEK campaign. *Geophysical Research Letters*, 25(11), 1801–1804. <https://doi.org/10.1029/97gl03448>

- Teunissen, P. J. (2020). GNSS precise point positioning. *Position, navigation, and timing technologies in the 21st century: integrated satellite navigation, sensor systems, and civil applications*, 1, 503–528. <https://doi.org/10.1002/9781119458449.ch20>
- Tsai, L. C., Su, S. Y., Schuh, H., Alizadeh, M. M., & Wickert, J. (2024). Seasonal–longitudinal variability of equatorial plasma bubbles observed by FormoSat-7/constellation observing system for meteorology ionosphere and climate II and relevant to the Rayleigh–Taylor instability. *Remote Sensing*, 16(13), 2310. <https://doi.org/10.3390/rs16132310>
- Tsunoda, R. T. (2010a). On equatorial spread F: Establishing a seeding hypothesis. *Journal of Geophysical Research*, 115(A12), A12303. <https://doi.org/10.1029/2010ja015564>
- Tsunoda, R. T. (2010b). On seeding equatorial spread F during solstices. *Geophysical Research Letters*, 37(5), L05102. <https://doi.org/10.1029/2010gl042576>
- Tsutsui, M., & Ogawa, T. (1973). HF Doppler observation of ionospheric effects due to typhoons. *Report of Ionosphere and Space Research in Japan*, 27(3), 121–123.
- Vadas, S. L. (2007). Horizontal and vertical propagation and dissipation of gravity waves in the thermosphere from lower atmospheric and thermospheric sources. *Journal of Geophysical Research*, 112(A6), A06305. <https://doi.org/10.1029/2006ja011845>
- Vadas, S. L., & Liu, H. I. (2009). Generation of large-scale gravity waves and neutral winds in the thermosphere from the dissipation of convectively generated gravity waves. *Journal of Geophysical Research*, 114(A10), A10310. <https://doi.org/10.1029/2009ja014108>
- Waldock, J., & Jones, T. (1984). The effects of neutral winds on the propagation of medium-scale atmospheric gravity waves at mid-latitudes. *Journal of Atmospheric and Terrestrial Physics*, 46(3), 217–231. [https://doi.org/10.1016/0021-9169\(84\)90149-1](https://doi.org/10.1016/0021-9169(84)90149-1)
- Wang, Y.-q., & Wu, C.-C. (2004). Current understanding of tropical cyclone structure and intensity changes—a review. *Meteorology and Atmospheric Physics*, 87(4), 257–278. <https://doi.org/10.1007/s00703-003-0055-6>
- Wood, A. G., Alfonsi, L., Clausen, L. B., Jin, Y., Spogli, L., Urbář, J., et al. (2022). Variability of ionospheric plasma: Results from the ESA swarm mission. *Space Science Reviews*, 218(6), 52. <https://doi.org/10.1007/s11214-022-00916-0>
- Xiao, S., Hao, Y., Zhang, D., & Xiao, Z. (2006). A case study on the detailed process of the ionospheric responses to the typhoon. *Chinese Journal of Geophysics*, 49(3), 546–551. <https://doi.org/10.1002/cjg2.867>
- Xiao, S., Shi, J., Zhang, D., Hao, Y., & Huang, W. (2012). Observational study of daytime ionospheric irregularities associated with typhoon. *Science China Technological Sciences*, 55(5), 1302–1304. <https://doi.org/10.1007/s11431-012-4816-7>
- Xiong, C., Stolle, C., & Lühr, H. (2016). The Swarm satellite loss of GPS signal and its relation to ionospheric plasma irregularities. *Space Weather*, 14(8), 563–577. <https://doi.org/10.1002/2016sw001439>
- Xu, S., Yue, J., Xue, X., Vadas, S. L., Miller, S. D., Azeem, I., et al. (2019). Dynamical coupling between hurricane matthew and the middle to upper atmosphere via gravity waves. *Journal of Geophysical Research: Space Physics*, 124(5), 3589–3608. <https://doi.org/10.1029/2018ja026453>
- Yang, Z., & Liu, Z. (2016). Observational study of ionospheric irregularities and GPS scintillations associated with the 2012 tropical cyclone Tembin passing Hong Kong. *Journal of Geophysical Research: Space Physics*, 121(5), 4705–4717. <https://doi.org/10.1002/2016ja022398>
- Yu, S., & Liu, Z. (2021). The ionospheric condition and GPS positioning performance during the 2013 tropical cyclone Usagi event in the Hong Kong region. *Earth Planets and Space*, 73, 1–16. <https://doi.org/10.1186/s40623-021-01388-2>
- Yu, S., Liu, Z., & Lee, T. C. (2022). Ionospheric disturbances observed from a single GPS station in Hong Kong during the passage of Super Typhoon Hato in 2017. *Space Weather*, 20(1), e2021SW002850. <https://doi.org/10.1029/2021sw002850>
- Zou, J., Li, X., Ren, Z., & Cao, J. (2024). Study of ionospheric equatorial plasma bubbles based on GOLD observations. *Journal of Geophysical Research: Space Physics*, 129(9), e2024JA032844. <https://doi.org/10.1029/2024ja032844>